CENTRO DE INVESTIGACIONES
EN OPTICA, A.C.

“STRATIGRAPHIC AND PIGMENT IDENTIFICATION IN CULTURAL HERITAGE ARTIFACTS USING TERAHERTZ AND NON-LINEAR SPECTROSCOPIES”

Thesis submitted to obtain the degree of Doctor of Science (Optics)

Presented by: Edgar Santiago Reyes Reyes

Thesis Advisor: Dr. Ramón Carriles Jaimes

Versión Definitiva.
Incluye cambios sugeridos por revisores
Vo.Bo. Ramón Carriles Jaimes.
31-Marzo-2025

León · Guanajuato · México
March 2025

Dedicado a mi familia. A Maria Esther, Urbano y Javier.

Agradecimientos

Quiero expresar mi más sincero agradecimiento al Dr. Ramón Carriles Jaimes, asesor de esta tesis, por su constante apoyo, orientación y valiosas sugerencias a lo largo de todo este proceso. Su experiencia y dedicación fueron fundamentales para llevar a buen término este trabajo. Al Dr. Enrique Castro Camus, cuya disponibilidad, acompañamiento y supervisión fueron esenciales para el desarrollo de esta investigación. A mi comité de seguimiento, el Dr. Edén Morales, el Dr. Gabriel Ramos y el Dr. Roberto Alarcón, quienes, a través de sus evaluaciones y observaciones, contribuyeron significativamente a mejorar la calidad y el enfoque de este trabajo. Agradezco además a mis sinodales por el tiempo dedicado a la revisión exhaustiva de este proyecto.

Al Dr. Jan C. Balzer, por su hospitalidad y asesoramiento técnico durante mi estancia académica en la Universidad de Duisburg-Essen. Al M.C. Tobias Kubiczek, por su tiempo y apoyo en la elaboración del Capítulo 4 de esta tesis, brindando perspectivas cruciales para su desarrollo. A la Dra. Kaori Fukunaga por su amabilidad al compartir los datos que ella y su equipo de investigación obtuvieron de la pintura *Homme au chapeau* de Pablo Picasso, los cuales se presentan en el capítulo 4 y forman parte de mi investigación.

Finalmente, quiero expresar mi gratitud al CONAHCYT por el apoyo recibido a lo largo de este proyecto a través de la beca 931264.

Publications and Presentations

- E.S. Reyes-Reyes, R. Carriles-Jaimes, E. D'Angelo, S. Nazir, C. L. Koch-Dandolo, F. Kuesker, P. U. Jepsen, E. Castro-Camus. Terahertz Time-Domain Imaging for the Examination of Gilded Wooden Artifacts. *Scientific Reports* **14**, 6261 (2024)

- E.S. Reyes-Reyes, R. Carriles-Jaimes, E. Castro-Camus. Algorithm for Determination of Cutoff Frequency of Noise Floor Level for Terahertz Time-Domain Signals. *Journal of Infrared, Millimeter, and Terahertz Waves* **43**, 847-856 (2022)

- E.S. Reyes-Reyes, R. Carriles-Jaimes, E. D'Angelo, S. Nazir, C. L. Koch-Dandolo, F. Kuesker, P. U. Jepsen, E. Castro-Camus. Investigation on a Religious Gilded Wooden Tablet using Terahertz Time-Domain Imaging. Poster presentation on *10th Optical Terahertz Science and Technology 2024 Conference*, Marburg, Germany, April 8-12, 2024.

- E.S. Reyes-Reyes, R. Carriles-Jaimes, E. Castro-Camus. Algorithm for Determination of Cutoff Frequency of Noise Floor Level for Terahertz Time-Domain Signals. Poster presentation on *48th International Conference on Infrared, Millimeter, and Terahertz Waves*, Montreal, Canada, September 17-22, 2023

- E.S. Reyes-Reyes, R. Carriles-Jaimes, E. Castro-Camus. Identificación de Pigmento por Detección de su Huella Espectral Utilizando Espectroscopía de Terahertz en el Dominio del Tiempo. Poster presentation on *Congreso TERAMEX 2023*, Querétaro, Mexico, June 8-9, 2023

Abstract

The application of non-destructive methods in cultural heritage research is crucial for preserving artifacts while obtaining valuable information about their preservation state. Terahertz (THz) radiation has proven effective in investigating the internal structure and composition of heritage objects, revealing underlying layers and hidden features. This aids in the development of informed conservation strategies for the long-term protection of cultural heritage. Additionally, multiphoton excited fluorescence (MPEF) offers a novel approach to studying pigments, enabling molecular-level characterization and revealing fluorescence signals from specific materials. This work presents an investigation using THz time-domain spectroscopy and MPEF, showcasing a stratigraphic study of a Russian icon and a Cubist painting through digital processing of THz signals using sparse deconvolution. We also demonstrate how the decay of spectral amplitude at noise level in the THz spectrum was used for pigment mapping in THz images. Finally, we highlight key results from the analysis of titanium dioxide, zinc sulfide, and cadmium sulfide using MPEF, where Second Harmonic Generation (SHG) and three-photon absorption phenomena were detected.

Contents

Chapter 1

Introduction

Art is considered a way for expressing our culture, beliefs, ideas, emotios or desires. When discussing tangible forms of art, such as paintings or sculptures, these objects serve as evidence of the intellectual and cultural evolution of our species over the years. Given the vital role that tangible art plays in history, culture and society, historians, conservators and restorers have the crucial mission of preserving these significant objects for future generations.

Over the last three decades, advancemenets in science and technology have led historians, curators and restorers to incorporate scientific techniques into their research methodologies. This approach helps them to understand the deterioration processes in various types of artifacts and implement suitable methodologies to prevent further degradation of artworks. From this perspective, scientific techniques provide a reliable approach to analyze cultural heritage (CH) objects, resulting in an interdisciplinary field known as *conservation science*. In this field, different areas of research collaborate, with the aim of preserving our cultural heritage in the most appropriate way.

Thanks to the scientific development in the last century, both theoretical and technological, our understanding of the nature of light has allowed us to apply the principles of optics and of radiation-matter interaction to the study of various objects, including artistic artifacts. In this context, this thesis focuses in the application of optics, specifically at terahertz (THz) and visible frequencies, to the evaluation of cultural heritage artifacts and materials by analyzing their optical response through their interaction with radiation.

1.1. Conservation of Cultural Heritage

Considering that this thesis is an interdisciplinary work, we find it necessary to introduce certain terms that will be consistently employed throughout this document but are not typically used in the field of optics. This will also help in establishing an appropriate context for the development of this work.

Cultural heritage, as defined by UNESCO [1], encompasses a wide spectrum of items and places with symbolic, historical, artistic, aesthetic, ethnological, anthropological, scientific, and social significance. Given the definition, there are three categories of cultural heritage, tangible, intangible and natural. Since this work focuses on the study of tangible CH, which includes artifacts, works of art and buildings, in the rest of this document when we mention CH we will refer exclusively to tangible CH.

On the other hand, *Conservation* refers to all measures taken to extend the life of tangible cultural heritage [2]. Conservation, in turn, includes *Preventive Conservation*, which aims to avoid and minimize future deterioration, *Remedial Conservation*, which refers to all measures aimed to stop current damaging processes or to reinforce the structure, and *Restorarion*, which refers to all actions applied directly to an item, aimed at facilitating its appreciation, understanding and use.

With these terms in mind, we can define *conservation science* as the field where scientific knowledge, methodologies, techniques, and technologies are applied to conservation efforts, thereby offering art conservators and restorers new perspectives into the analysis of artistic artifacts. Furthermore, it provides modern technological tools capable of analyzing objects and buildings without the risk of damaging them, utilizing non-destructive and non-invasive techniques. Thus, conservation science emerges as a bridge between traditional art restoration and modern scientific advances.

1.2. Electromagnetic Radiation Applied in Cultural Heritage Science

One of the earliest effors to apply scientific principles to the study of historical objects emerged within the field of *Archeometry*, a term proposed by Martin Aitken and Christopher Hawks in the mid-1950s, as an interdisciplinary field for the study of archeology with different scientific perspectives [3]. Since then, different branches of physics have been applied to study objects of interest in other fileds, including optics and photonics for analyzing cultural artifacts.

Generally speaking, the entire electromagnetic (EM) spectrum can be used to analyze and characterize all types of materials and objects, since each range of frecuencies interact in a specific way with matter. For this reason, experts can select the most suitable technique using a specific range of the EM spectrum based on their research objectives, with the primary goal of preserving the integrity of the work under study. The following is a brief description of the four most commonly used techniques in conservation science related to electromagnetic radiation.

X-ray Fluorescence (XRF) is one of the most widely used techniques for element identification in conservation science. In this technique, the sample is irradiated with high-energy X-ray photons, which ionize electrons in the inner orbitals of atoms present in the sample. Then, electrons in higher energy orbitals decay to lower energy states, filling the "holes" created by the ionized electrons, thus producing a high-energy radiative emission. Photons generated in this process are analyzed, since each chemical element excited by X-ray radiation emits photons with specific energies. This makes it possible to identify the chemical composition of different samples. Currently, Macro-XRF (MA-XRF), together with the development of portable XRF devices allow to construct chemical element maps in easel paintings [4, 5, 6], panel paintings [7, 8], icons [9, 10], among many others.

Ultraviolet-Visible (UV-Vis) spectroscopy is another technique used to study artistic objects, which includes measurements of transmitance, reflectance and fluorescence, using the UV-Vis regions of the EM spectrum (200 nm - 750 nm, typically). Since most molecules absorb energy in the UV-Vis range, it is possible to analyze and identify different organic compounds, allowing to study organic colorants in manuscripts [11, 12, 13, 14], textiles [15, 16],and even mosaics [17].

Raman spectroscopy is useful for molecular identification by analyzing the response of chemical bonds to light, using lasers in the Near Infrared (NIR), visible or UV range as excitation sources. Features such as its high spatial resolution, capability to analyze both organic and inorganic molecules, and non-destructive nature make Raman spectroscopy a versatile and indispensable analytical technique in conservation science. In addition, the development of portable Raman instruments has allowed for *in situ* analysis [18, 19] , which is ideal for artifacts that cannot be transported to the laboratory for study. Raman spectroscopy is one of the most used technique for pigment identification, providing crucial information about the materials used by artists throughout history [20, 21, 22, 23].

Fourier Transform Infrared Spectroscopy (FTIR spectroscopy) is another important technique, where IR radiation (2.5 μm - 25 μm) is used to analyze and identify both organic and inorganic chemical compunds. As a vibrational spectroscopic tecnique, FTIR spectroscopy offers a practical method to analyze pigments, as their chemical composition is associated with a specific vibrational patterns in the IR spectrum. Some other applications in CH science using FTIR spectroscopy include identifying binding media [24], analysis of coatings [25], study of deterioration in objects [26], and cross-sectional analysis from artistic samples [27, 28].

The list of scientific techniques with application in the field of conservation continues to grow, year by year, such as the recent approach offered by nonlinear optics to study historical and artistic objects [29, 30, 31], which invites further exploration of new optical approaches in the study of CH objects.

1.3. THz radiation and Conservation Science

Since the first demonstrations of sub-picosecond light pulse generation in the late 1980s, THz technology emerged as a innovative technique that has found applications in several fields of study, including the analysis of artistic objects. Before discussing some applications of THz spectroscopy in cultural heritage science and why it has become a complementary technique in this field, let us first define what THz radiation is.

We usually refer to THz radiation as the frequency range of the electromagnetic spectrum between 0.3 THz and 10 THz ($\lambda \sim 1\,\mathrm{mm}$ - $0.03\,\mathrm{mm}$), known as "terahertz band". At these frequencies, light exhibits unique properties, as THz radiation is highly reflective in metals, can peneterate optically opaque materials and is strongly absorbed by water molecules. In addition, the non-iozing nature of THz radiation, combined with its high chemical selectivity, makes it an interesting area of research.

In the past, accessing this band was challenging; however, this scenario changed when in 1988 photoconductive antennas were introduced for generating and detecting subpicosecond pulses [32], thus enableing *Terahertz Time-Domain Spectrospy* (THz-TDS). Since then, THz-TDS applications have been expanded to diverse fields of study, including medicine [33, 34, 35], engineering [36, 37], agronomy [38, 39], architecture [40, 41, 42], pharmaceutics [43, 44], among others.

Not surprisingly, THz-TDS also has applications in conservation science, given its features. Since some chemical compounds exhibit *spectral fingerprints* at THz frequencies, it is possible to idenfity certain pigments [45, 46, 47]. In addition, given that THz radiation can penetrate dielectric materials, it is possible to perform cross-sectional analysis in a non-destructive way, allowing the study of layer distributions on multilayered samples [48, 49]. There is an extensive list of objects that have been analyzed and studied by means of THz-TDS, including easel paintings [50], wall paintings [51, 52], panel paintings [53, 54], stone artworks [55], buildings [56], just to mention a few.

It is worth mentioning that in cultural heritage research, analyzing objects typically involves using various measurement techniques to obtain objective information that contributes to the historical record or aids in successful restoration. Recently, THz-TDS has been increasingly adopted by scientists in this field as a complementary tool to existing methods, making this technique a valuable addition to the range of available tools for the study and conservation of CH.

1.4. Objectives

Given the advantages of THz spectroscopy for research in cultural heritage sciences, the aim of this work focuses on the applications of THz-TDS for analysis of objects of artistic interest. Terahertz Time-Domain Imaging (THz-TDI) is also applied for analysis of areas of interest in paintings and objects, allowing to analyze cross-sectional images or *B-Scans*. This work also shows the role that data processing plays for a correct interpretation of THz signals. In addition, we present a first approach of pigment identification using multiphoton exited fluorescence (MPEF) microscopy in three pigments of historical interest.

With the above in mind, in Chapter 2 we discuss the theory behind THz-TDS and THz-TDI, briefly explaining how THz radiation is generated and recorded in the time-domain and how optical parameters are calculated.

In Chapter 3, we introduce a data processing method for calculating the usable bandwidth in THz signal. The algorithm is based on smoothing and multiplying spectra by funcions of n-powers, generating a minimum at a frequency where the amplitude of usable bandwidth decays to the noise floor.

In Chapter 4, we present the results of our analysis of two artworks: a Russian icon titled *Our Lady of Kazan* and an oil painting titled *Homme au Chapeau* [57] using THz-TDI. We apply the algorithm for calculating the cutoff frequency, which helps us in generating pigment maps. Additionally, we show the results of applying *sparse deconvolution*, a digital processing technique that helps recover overlapping echoes in THz signals.

Chapter 5 focuses on introducing a novel imaging technique known as *3D THz-TDS Synthetic Aperture Radar (SAR) Imaging*, which enables the scanning of complex-shaped samples using THz radiation. We apply this method to study the stratigraphy of cultural heritage artifacts.

In Chapter 6, we shift to nonlinear optics, investigating its role in pigment characterization. Here, we examine three pigments of interest, reporting on the phenomenon of multiphoton absorption and fluorescence in one pigment and identifying evidence of second harmonic generation (SHG) in two others.

Finally, Chapter 7 concludes the thesis by summarizing the advantages and limitations of each technique presented.

Chapter 2

Terahertz spectroscopy

THz spectroscopy was introduced in the late 1980s as an innovative technique using sub-picosecond pulses containing THz frequencies . The generation and detection of THz beams were achieved through the development of Photoconductive Antennas (PCA), devices that are still used in THz spectroscopy to this day. This chapter introduces the principles of THz spectroscopy, technique used to analyze the response of a wide range of materials at THz frequencies. Additionally, THz spectroscopy allows to analyze echoes reflected from buried surfaces to examine the inner structure of multilayered objects, making it valuable in conservation science due to its non-invasive nature. It is important to mention that this work exclusively centers on PCA as mechanism for generating and detecting THz radiation since the measurements presented in this thesis were performed using THz systems employing PCA technology.

2.1. Generation and Detection of THz Radiation

PCA is one of the most widely methods used for both, THz generation and detection in THz spectroscopy. These small devices can operate at room temperature, are very compact and emit THz pulses efficiently. The fabrication of PCAs in the late 1980s started a revolution in THz radiation research and its applications in the following decades [58, 59].

In essence, PCA refers to a metal dipole antenna integrated onto a semiconductor subtrate, whose conductivity changes when exposed to light. Small electrodes, located on its surface are connected to a DC bias voltage and are separated by an active region known as the *antenna Gap*. Ultra-short optical pulse are indispensable for its operation as will be explained later.

To this day, a standard way to generate THz radiation is using *mode locked lasers*. Tipically, mode locked lasers use a sapphire crystal doped with Titanium ions (Ti:Sapphire) as active medium. The broad gain spectrum of this active medium (ranging from 650 to 1100 nm) is crucial for generating ultrashort pulses, as extremely short time pulses require broad spectral bandwidths, given by the time-bandwidth product $\Delta\nu \simeq 0.44/\tau_p$, where $\Delta\nu$ is the bandwidth and τ_p is the pulse duration. Moreover, the term mode locked refers to the synchronization of phase of multiple different modes of the laser cavity. When these modes are forced to have equal fixed phases, they will interfer at specific periodic times, resulting in a train of light pulses as output. Typically, mode-locked lasers produce pulses on the order of tens of femtoseconds [60].

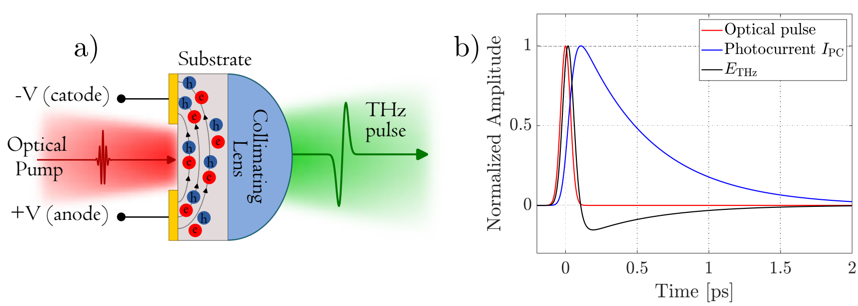

Figure 2.1: THz radiation generation process by means of PCA.

In the generation of THz radiation, fs pulses play a vital role since they act as optical switches by illuminating the gap of the PCA, and thus allowing the semiconductor substrate to generate free carriers (electrons and holes), assuming that the energy of the photons is larger than the bandgap of the material (see Fig. 2.1 a). Due to the DC bias voltage applied to the electrodes, the free carriers generated by the pulse are accelerated from the anode towards the cathode. After this short acceleration, the charge density on the substrate decreases as free carriers begin to recombine. The accelation and deceleration, which are in subpicoseconds scale, generate pulses of radiation at THz frequecies. The THz electric field E_{THz} generated can be written as

$$E_{\mathrm{THz}}(t) \propto \frac{dI_{\mathrm{PC}}(t)}{dt}, \tag{2.1}$$

where I_{PC} is the photocurrent in the PCA gap. Fig. 2.1 b) shows the behavior of E_{THz} as a function of I_{PC} [61]. The THz beam propagates along the axis of the optical pulse.

One of the most widely used substrates in PCA is low-temperature-grown gallium arsenide (LT-GaAs) due to its short carrier lifetime (1-10 ps) and carrier mobility (120-150 cm^2/V·s). These properties allow it to generate picosecond and femtosecond electric pulses within the THz spectrum when optically excited [62, 63].

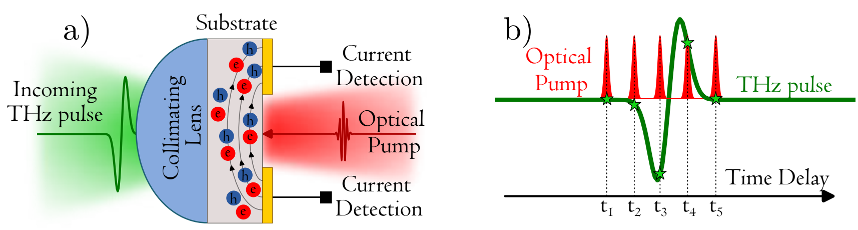

Figure 2.2: Detection of THz radiation using PCA.

On the other hand, for the detection of THz radiation, the optical pulse, initially divided by a beam splitter, is incident on the antenna gap of another PCA, now operating as a receiver device. Similar to the transmitter, free carriers are generated in the substrate by the optical pulse as Fig 2.2 a) shows. However, unlike the emitter PCA, the receiver PCA is not connected to a DC bias voltage, instead the THz pulse to be measured is focused onto the dipole antenna, inducing a transient bias voltage between the electrodes which can be measured with a lock-in amplifier. Considering that the lifetime of the photoexcited carrier is of the order of femtoseconds, the photocurrent generated in the PCA will be proportional to the transient bias voltage at the time the optical pulse is injected into the substrate. Using a delay stage, we can change the arrival time between the THz pulse and the optical pulse, allowing us to record the photocurrent at different time delays and mapping the complete THz pulse as illustrated in Fig. 2.2 b). The photocurrent is expressed as [61]

$$J(t) = \int_{-\infty}^{t} \sigma_s(t-t') E_{\mathrm{THz}}(t') dt', \tag{2.2}$$

where $J(t)$ is the photocurrent and $\sigma_s(t)$ is the transient surface conductivity of the PCA substrate. As we can see from Eq.2.2, the photocurrent is a convolution between the THz field $E_{\mathrm{THz}}(t)$ and $\sigma_s(t)$. If we take the fourier transform, we obtain that the spectral distribution of $J(t)$ does not contain the same espectral distribution of $E_{\mathrm{THz}}(t)$, as $\sigma_s(t)$ limits the distribution of frequencies.

With all the above in mind, a typical THz time-domain system is show in Fig. 2.3. The spectroscopy technique using time-resolved THz fields measurements is known as Terahertz Time-Domain Spectroscopy (THz-TDS). As well as in other spectroscopic techniques, in THz-TDS we analyze the THz signal from a sample against a reference signal in order to calculate the optical parameters correspongind to the sample.

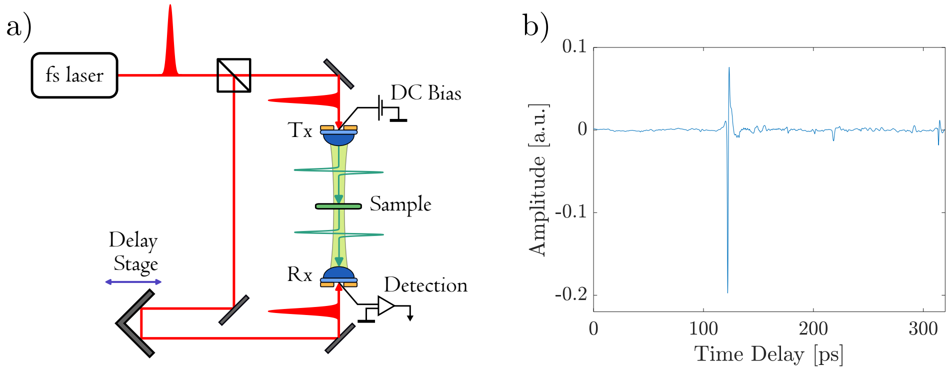

Figure 2.3: a) THz Time-Domain system. b) Experimental reference measurement

2.2. Optical Parameter Calculation

To calculate the optical parameters of a sample, an electric field $E_{\text{ref}}(t)$ propagating in free space is recorded as a reference. The sample is then placed between the transmitter and the receiver and the THz beam transmitted through the sample E_{sam} is recorded. Using the Fourier transform, we obtain their spectral distributions and phases as $\tilde{E}_{\text{ref}}(\omega) = A_{\text{ref}}(\omega)e^{i\phi_{\text{ref}}(\omega)}$ and $\tilde{E}_{\text{sam}}(\omega) = A_{\text{sam}}(\omega)e^{i\phi_{\text{sam}}(\omega)}$. If we divide $\tilde{E}_{\text{sam}}$ by $\tilde{E}_{\text{ref}}$, we obtain the complex transmission coeeficient $\tilde{T}(\omega)$, expressed as

$$\tilde{T}(\omega) = \frac{\tilde{E}_{\text{sam}}(\omega)}{\tilde{E}_{\text{ref}}(\omega)} = \frac{A_{\text{sam}}(\omega)}{A_{\text{ref}}(\omega)} e^{i(\phi_{\text{sam}}(\omega) - \phi_{\text{ref}}(\omega))}. \tag{2.3}$$

Furthermore, the complex transmission coefficient can be written in terms of the complex refractive index $\tilde{n} = n + i\kappa$ and the Fresnel transmission coefficients $t_{12} = 2/(\tilde{n}+1)$, $t_{21} = 2\tilde{n}/(\tilde{n}+1)$ as

$$\tilde{T} = t_{12}(\omega)t_{21}(\omega)e^{i\frac{\omega d}{c}(\tilde{n}(\omega)-1)}\text{FP}(\omega), \tag{2.4}$$

where d is the thickness of the sample, c is the speed of light and FP(ω) is the Fabry-Perot term associated with multiple internal reflections. This term can be approximated to 1 by avoiding multiple reflections between the interfaces of the sample. By combining 2.3 and 2.4, we obtain $n(\omega)$ and $\kappa(\omega)$ as

$$\begin{aligned} n(\omega) &= 1 + \frac{c(\phi_{\text{sam}}(\omega) - \phi_{\text{ref}}(\omega))}{\omega d}, \\ \kappa(\omega) &= -\frac{c}{2\omega d} \ln\left[\frac{1}{t_{12}(\omega)t_{21}(\omega)} \frac{A_{\text{sam}}(\omega)}{A_{\text{ref}}(\omega)}\right]. \end{aligned} \tag{2.5}$$

Using $\kappa(\omega)$ from Eq. 2.5, we can calculate the absorption coefficient as

$$\alpha(\omega) = \frac{2\omega\kappa(\omega)}{c}. \tag{2.6}$$

Since THz-TDS measures amplitude and phase information, it is possible to calculate both the absorptive and refractive properties of the sample.

2.3. Multilayered Samples and reflection measurements

For analyzing multilayered media, THz-TDS is a revelant technique as THz radiation penetrates dielectric materials in a non-destructive way. Since stratigrapic studies are typically performed in reflection geometry, consider Fig. 2.4, which shows a two-layer system. This system consists of layers with thicknesses d_1 and d_2, and complex refractive indices $\tilde{n}_1$ and $\tilde{n}_2$, respectively. The layers have flat and parallel faces. In this example, we assume that the sample is surrounded by air with a complex refractive index $\tilde{n}_0$; a THz pulse denoted by $E_i(t)$ propagates through free space, traveling perpendicular to the surface of the sample.

In general, the incident pulse $E_i(t)$ will be partially reflected and transmitted at each interface, so the total reflected pulse $E_r(t)$, in terms of the Fresnel coefficients, will be

$$E_r(t) = r_{01}E_i(t) + t_{01}r_{12}t_{10}P_1E_i(t) + t_{01}t_{12}r_{20}t_{21}t_{10}P_2E_i(t), \tag{2.7}$$

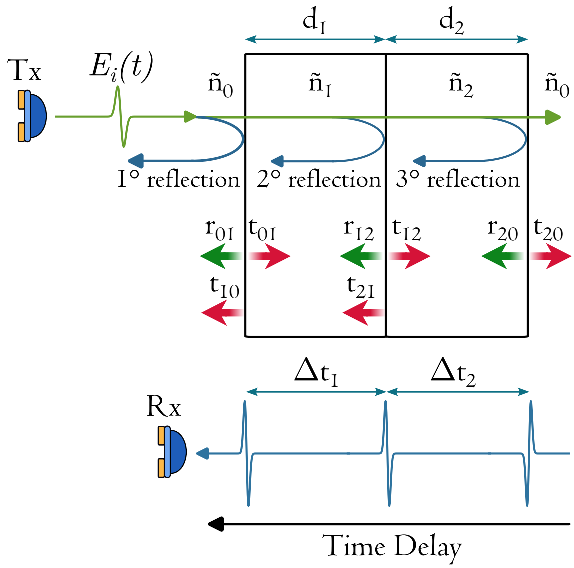

Figure 2.4: THz pulses reflected from a two layer system.

where the complex reflection and transmission Fresnel coefficients traveling from a medium a to a medium b at normal incidence are

$$r_{ab} = \frac{\tilde{n}_a - \tilde{n}_b}{\tilde{n}_a + \tilde{n}_b}, \tag{2.8}$$

$$t_{ab} = \frac{2\tilde{n}_a}{\tilde{n}_a + \tilde{n}_b}, \tag{2.9}$$

where $P_1 = e^{-2ikd_1\tilde{n}_1}$,$P_2 = e^{-2ik(d_1\tilde{n}_1+d_2\tilde{n}_2)}$ with $k = \omega/c$, represent the propagation of $E_i(t)$ through the layers.

From Eq. 2.8, we note that, if $\tilde{n}_a > \tilde{n}_b$, then $r_{ab} > 0$; however if $\tilde{n}_a < \tilde{n}_b$, then $r_{ab} < 0$. This is an interesting result as in the later case, the polarity of the reflected pulse from the corresponding interface will shift.

One of the advantages of analyzing multilayer structures by THz-TDS is that the reflected pulse is recorded in the time domain, so we can calculate the thickness of individual layers, as the time between echoes is proportional to the distance between interfaces as

$$\Delta t = 2nd/c, \tag{2.10}$$

where n is the refractive index of the layer, offering a practical way to study layer distributions.

Another way to analyze a multilayer system is by a convolution. Since we record reflections of the reference pulse from each interface, we can model the train of echos as a convolution of the reference pulse $E_i(t)$ and the impulse response function $h(t)$ as

$$E_r(t) = \int_{-\infty}^{\infty} E_i(\tau) h(t-\tau) d\tau = E_i(t) \otimes h(t). \tag{2.11}$$

In a multilayered system, the impulse response function $h(t)$ would correspond to a collection of Dirac deltas $\delta(t-\tau)$, where each Dirac delta represents a interface in the sample, as Fig. 2.5 shows.

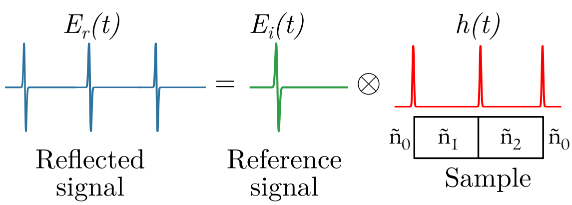

Figure 2.5: The recoded signal reflected from a multilayered sample can be expressed as a convolution between a reference signal $E_i(t)$ and the impulse response function $h(t)$.

This approach, as we will see in the following chapters, will allow us to recover the impulse response function in complex samples where the reflections from interfaces overlap, helping to remove the ambiguity in the layer distribution calculation.

2.4. THz Imaging

THz-TDS also offers the capability of generating images, a technique called *Teraherz Time-Domain Imaging* or THz-TDI. In this technique, both the transmitter and receiver are placed on a XY plataform in reflection geometry, as Fig. 2.6 a) shows. An area of interest is scanned by recording the train of echoes of the THz beam reflected by the sample, resulting in a data cube, where the XY plane represents the pixels of the image and the Z axis represents the amplitude of the THz beam as function of the time, as Fig. 2.6 b) illustrates.

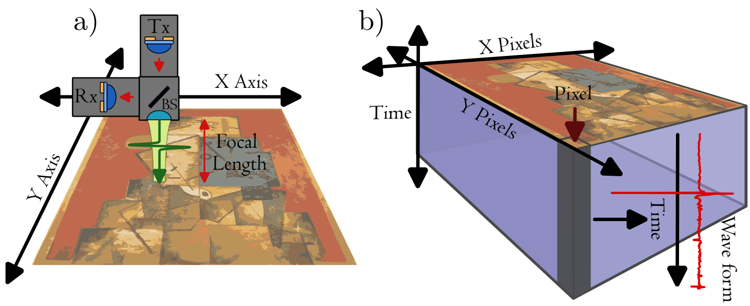

Figure 2.6: a)THz image data recording. A transceiver head is located in a XY platform to scan an area of interest in reflection geometry. b) THz image. Each pixel of a THz image corresponds to a waveform or trace of the echoes reflected by the object.

THz-TDI represents an important tool in conservation science for studying the inner structure of objects of interest, both in the time and spectral domains. In a THz image, each pixel contains temporal information in depth, allowing us to obtain cross-sectional images, or B-scans, by selecting the temporal information along the Z-axis of a row or column of pixels. Fig. 2.7 illustrates how we obtain B-scans from a THz image.

The THz image correspond to an oil painting on canvas by Pablo Pi-

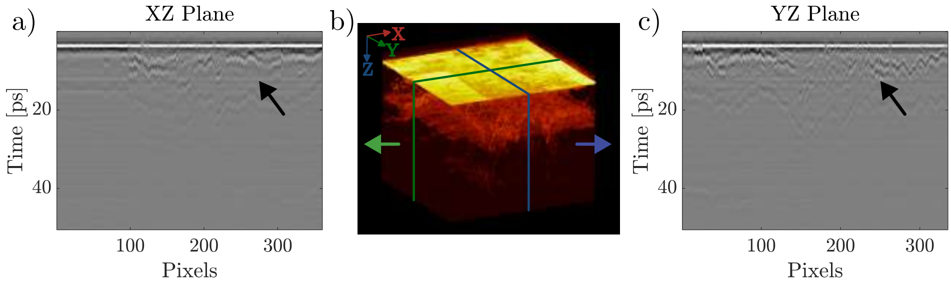

Figure 2.7: a) B-scan from the green line in the THz image. b) 3D THz image recorded from "Homme au chapeau" by Pablo Picasso [57]. c) B-scan from the blue line in the THz image. The arrows show the complex stratigraphic distribution beneath the paint surface.

casso titled "Homme au chapeau", part of the collection of Tokyo Station Gallery, Japan [57]. The THz image was scanned by Dr. Kaory Fukunaga's group. As we can see, the layer distribution is easily distinguished on the B-scans in both the XZ and YZ planes, indicated by arrows. In the next chapter will explore how a digital processing technique can enhance the accuracy and detail of stratigraphic analysis in a secondary study on this artwork.

An important factor to keep in mind in THz-TDI is the use of lenses for focusing the THz radiaion. First, the THz beam is diffraction-limited. Considering the THz beam as a Gaussian beam, the diameter of the beam $2\omega_0$ is expressed as

$$2\omega_0 = \frac{4}{\pi}\frac{c}{f}\frac{f_l}{D}, \tag{2.12}$$

where c is the speed of light, f_l is the focal length, D the diameter of the lens and f is the frequency. From Eq. 2.12, we note that the diameter of the beam is larger for low frequencies than for high frequencies. This information is crucial for determining the resolution of the THz image when choosing a optimal scanning distance between raster pixels.

Secondly, the focal plane. In a reflection measurement, the sample must be located at the focal point of the transmitter/reciver, as the Signal-to-Noise Ratio (SNR) decreases if the sample is not properly aligned. Ideally, analyzing samples with completely flat surfaces is highly recomeded, since the image quality of samples with complex shapes decreases. This problem will be addressed in the next chapter.

Chapter 3

Determination of usable bandwidth in THz signals

As discussed in Chapter 2, THz-TDS uses photoconductive antennas to generate THz monopulses with a full width at half maximum (FWHM) of a few picoseconds in the time-domain. These pulses contain a broad frequency range, typically from approximately 300 GHz to 2-5 THz, depending on the system. This frequency distribution depends on specific factors, such as the lens used for focusing the THz radiation, the system alignment, and, of course, the analyzed sample. These factors influence the range of frequency components in THz signals, also known as the *usable bandwidth*.

Tipically, the calculation of the usable bandwidth is done empirically when the volume of analyzed spectra allows it. However, when a large volume of spectra is analyzed, such as in a THz image containing hundreds of thousands of signals, it becomes necessary to automate the calculation of the usable bandwidth. In this chapter, we introduce an algorithm for determining the usable bandwidth in THz spectra. The algorithm identifies the frequency at which the spectral amplitude decays to the noise floor in the frequency-domain.

3.1. Theory

In THz pulsed spectroscopy, the spectral amplitude decreases at high frequencies until it becomes indistinguishable from the noise floor [64], such as indicated by Fig. 3.1 b). Although the frequency-domain covers 5 THz, the usable bandwidth only covers a fraction of the total bandwidth. In this analysis, the cutoff frequency defines the usable bandwidth for each spectrum. In other words, the cuttoff frequency indicates the boundary between the usable bandwidth and noise floor. For this analysis, we begin by considering the function

$$g_{\mathrm{THz}}(t) = (t - t_0)e^{-(t-t_0)^2/\sigma^2} \tag{3.1}$$

as an analytical model of a single-cycle terahertz pulse in the time-domain. For this analysis, we take $t_0 = 0$ and $\sigma = 1$ ps; by adding white noise n_w, the pulse is expressed as $g(t) = te^{-t^2} + n_w$. Taking the fouier transform we obtain

$$G(\omega) = -i\pi^{\frac{3}{2}}\omega e^{-\frac{\omega^2\pi}{2}+N}, \tag{3.2}$$

where N is the Fourier transform of n_w which is constant for white noise and represents the noise floor in the frequency-domain.

At low frequencies, $G(\omega)$ increases proportionally to ω . However, as ω increases. $G(\omega)$ will decrease exponentially as $e^{-\frac{\omega^2\pi}{2}}$; At some frequency, which we call cutoff frequency ω_c, the spectral amplitude has values comparable to N. Beyond ω_c, the first term in Eq. 3.2 becomes negligible and, therefore $G(\omega) \approx N$.

If we now multiply $G(\omega)$ by ω as $G_1(\omega) = \omega G(\omega)$, this expression will exhibit two different behaviors bounded by ω_c. For $\omega < \omega_c$, the first part of $G_1(\omega)$ will have an ω^2 multiplying the exponential, resulting in a gradual

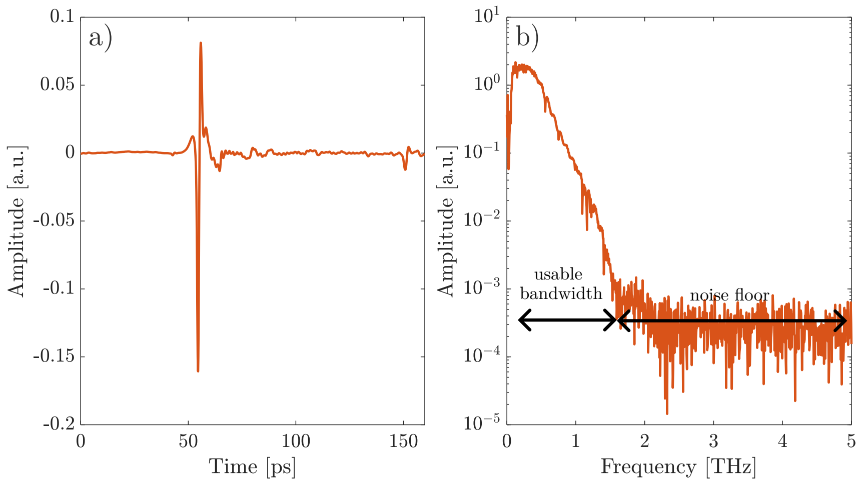

Figure 3.1: a) THz waveform. b) THz spectrum calculated using the Fourier transform. The usable bandwidth in the spectrum ranges approximately from 100 GHz to 1.6 THz.

decay of the spectral amplitude. However, for $\omega > \omega_c$, the frequency range corresponding to the noise floor in the spectrum, $G_1(\omega)$ will behave as a linearly increasing function ωN, generating a minimum at the frequency ω_c.

In general, we observed the same behavior with $G_n(\omega) = \omega^n G(\omega)$, generating minima at

$$\frac{1}{n} e^{-\omega^2 \pi} \left[\pi^4 \omega^4 - (n+1)\pi^3 \omega^2 \right] = N^2. \tag{3.3}$$

In practice, if we multiply a spectrum $G(\omega)$ by ω, it is sufficient to estimate the minimum, as shown in Fig 3.2.

As we can see from Fig. 3.2, the frequency range corresponding to the noise floor grows faster as n increases. In other words, as n increases, the cutoff frequency ω_c decreases. However, the shift in ω_c with increasing n is not significant in this case. The shift using $G_1(\omega)$ and $G_4(\omega)$ is

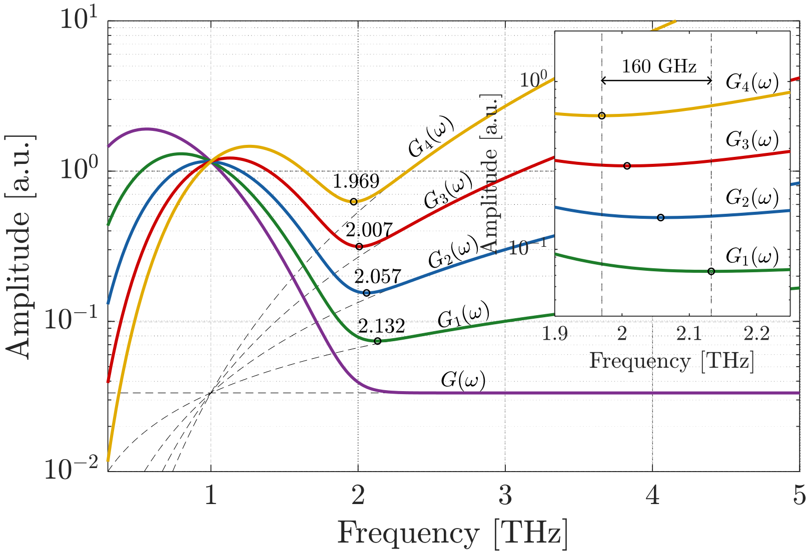

Figure 3.2: Estimation of ω_c using $G_n(\omega) = \omega^n G(\omega)$ for $n = 1, 2, 3, 4$ and $N = 0.0334$. ω_c is indicated by a circle in each plot. Dashed lines represent $\omega^n N$

only 160 GHz, representing 8.4% of the total bandwidth in the example, as shown in the inset of Fig. 3.2.

3.2. Experimental analysis

When analyzing experimental spectra, we must consider the random oscillations of the noise floor that influence the performance of the method applied in our investigation, leading to a miscalculation of ω_c. This issues can be aaddressed with appropriate smoothing.

The above consideration is included in the following analysis, where spectra from three different spectrometers were analyzed, corresponding to the spectra shown in Fig. 3.3 in the same order:

a) A home-built spectrometer based on a Ti:Sapphire oscillator with a central wavelenght of 800 nm with a pulse duration of 35 fs, using a SI-GaAs PCA as emitter and a 1 mm ZnTe crystal-based electro-optic sensor as detector, recording 100 points over 6.6 ps delay.

b) A commercial TDS system based on an Yb:fiber laser centered at 1064 nm with a pulse duration of 90 fs, using a PCA both as emitter and detector, recording 1600 points over 160 ps.

c) A commercial TDS system based on an Yb:fiber laser centered at 1064 nm with a pulse duration of 90 fs, using a PCA both as emitter and detector, recording 8000 points over 800 ps.

A set of reference measurements in transmission configuration were performed following the same methodology. However, we will show only one case for each system, as the result of the complete data set were comparable. The smoothing applied to the data was done using the moving average method, with a width w_s corresponding to 3% of the complete number of points recorded.

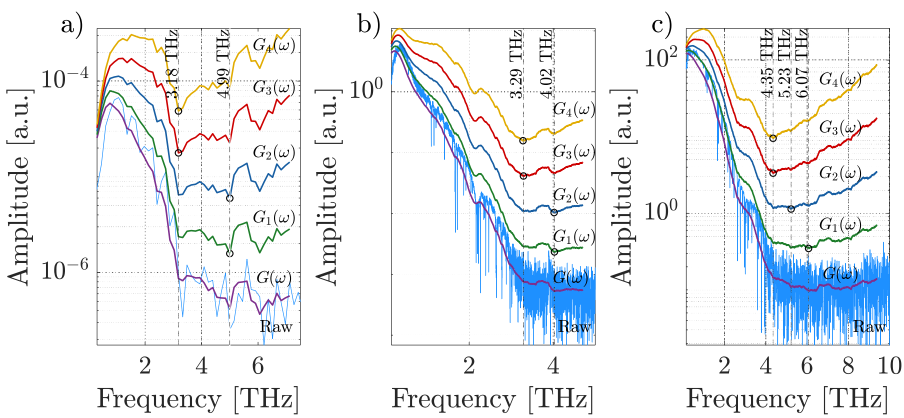

Figure 3.3: Calculation of ω_c on references experimental data using $G_n(\omega) = \omega^n G(\omega)$ for $n = 1, 2, 3, 4$.

As shown in Fig. 3.3 a), there is no difference using $G_1(\omega)$ and $G_2(\omega)$, with $\omega_c = 4.99$ THz; however, it is evident that the cutoff frequency should be lower. By increasing n to 3, ω_c decreases at 3.18 THz, providing a more consistent result. Using $G_4(\omega)$, the cutoff frequency is calculated to be the same frequency as with $G_3(\omega)$.

In the case of Fig. 3.3 b), the small peak centered at 3.93 THz is an artifact of the THz system, leading to a miscalculation of the cutoff frequency with $\omega_c = 4.09$ THz for both $G_1(\omega)$ and $G_2(\omega)$. On the other hand, both $G_3(\omega)$ and $G_4(\omega)$ give $\omega_c = 3.29$ THz, a result that is more in line with the visual estimate.

For the last spectrum, shown in Fig. 3.3 c), we obtained three different values of ω_c. Similiar to the other systems, both $G_3(\omega)$ and $G_4(\omega)$ yield the same value with $\omega_c = 4.35$ THz. Considering all this information, the analysis suggests that it is sufficient to use $G_3(\omega)$ to calculate the cutoff frequency in a reference spectrum.

As previously mentioned, smoothing is another crucial aspect of our processing, as it simplifies the determination of the cutoff frequency by eliminating random fluctuations in the experimental signal. To determine an appropriate level of smoothing to apply to THz signas, Fig. 3.4 shows the spectra and their cutoff frequencies calculated using different values of w_s , and by multiplying the smoothed spectrum by ω^3. Considering that the analysis included Savitzky-Golay, moving average and non-centered moving average method, with the latter giving the best results, only the results using the non-centered moving average method are shown.

For a spectrum recorded from a metallic flat surface in reflection geometry, shown in Fig. 3.4 a), the ω_c calculated using a smoothing width $w_s = 3\%$ of the total elements of the signal was $\omega_c = 2.1$ THz, decreasing only 107 GHz for $w_s = 15\%$. However, for the spectrum in Fig. 3.4 b), which correspond to a metallic sample with an irregular face, results indicate no further changes for $w_s > 9\%$, giving $\omega_c = 2.72$ THz. Based on these results, we established values for $w_s \geq 6\%$ and $n \geq 3$ for processing

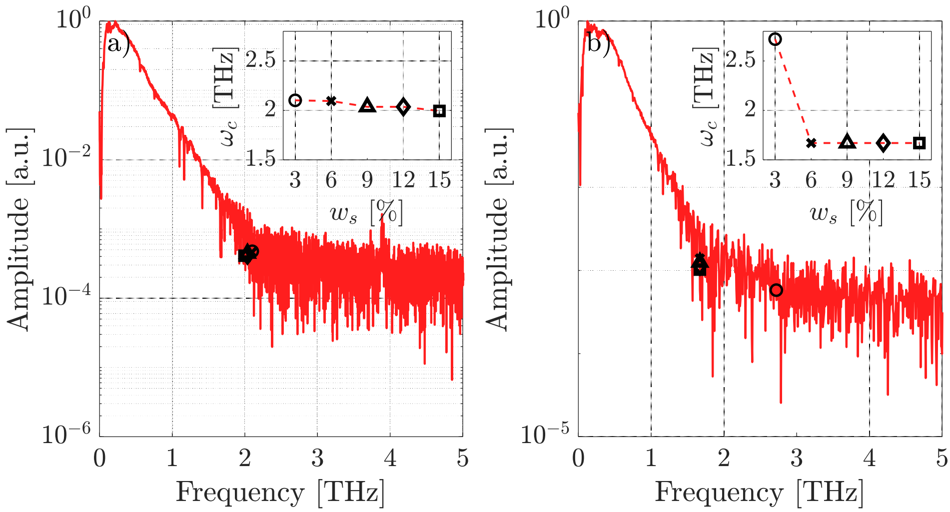

Figure 3.4: Calculation of ω_c using $w_s = 3\%, 6\%, 9\%, 12\%$ and 15% for $n = 3$, applied to spectra corresponding to a a) flat metallic surface and an b) irregular metallic surface. Insets show ω_c as a function of w_s

most spectra, with no significant changes in the calculation of ω_c.

Additionally, we were also interested in analyzing signals from samples placed out of the focal plane of the spectrometer which affects the range of the usable bandwidth. For this analysis, signals from a high-density polyethylene (HDPE) sample were recorded in reflection configuration. Using a 3 - inch focal length lens, the sample was placed at the focal point and moved ± 12 mm along the optical axis, recording waveforms every 3 mm. As the sample moves away from the focal point, the amplitude spectrum decays non-uniformly across the entire band, leading to a decrease in the effective bandwidth. Cutoff frequencies were calculated using $w_s = 6\%$ and $n = 3$. The results are shown in Fig. 3.5 a).

As we expected, the highest ω_c was 1.66 THz, corresponding to the sample placed at the focal point. The same ω_c was calculated when the sample was displaced +3 mm, which is within the Rayleigh length of the

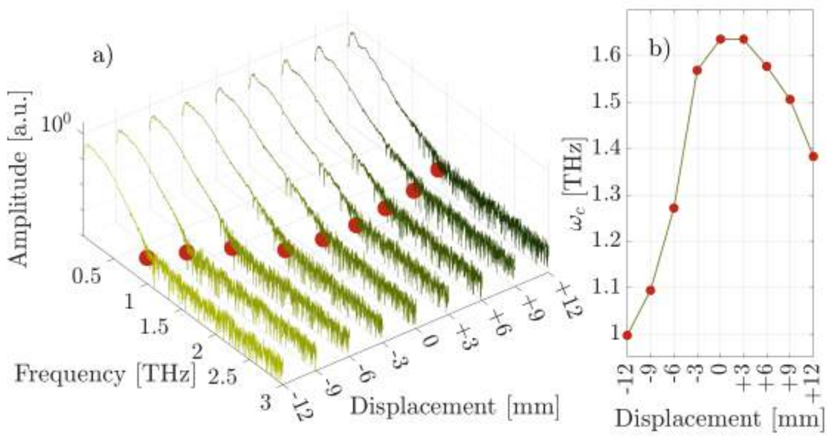

Figure 3.5: a) Spectra of a HDPE sample. The sample was displaced ± 12 mm out of the focal length, recording the reflected signal every ± 3 mm. Red circles indicate the cuff-off frequency calculated in each position. b) ω_c as a function of the sample displacement.

THz beam. Moreover, ω_c decreases as the sample moves away from the focal point of the lens, falliing to 1 THz for -12 mm. This behaivor is shown in Fig. 3.5 b) where ω_c is shown as function of sample displacement.

3.3. Implementation of the estimation of ω_c in noisy and HgS spectra

In order to evaluate the performance of the algorithm in different experimental scenarios, we focused on two specific cases, starting with the analysis of spectra with poor usable bandwidth. This will allow us to identify and discard extremely noisy signals from the THz image, ensuring that only spectra with a good SNR in the frequency range of interest are analyzed. The second case involves analyzing spectra that contain the mercury sulfide (HgS) or vermilion, a reddish pigment with historycal and artistic relevance. Additionally, this pigment has the characteristic of exhibiting an spectral fingerprint at 1.14 THz. This spectral feature will allowing us to validate the accuracy of the method. The results of this analysis are shown in Fig. 3.6 using a smoothing width $w_s = 6\%$ and $n = 3$.

In order to evaluate the performance of the algorithm in different experimental scenarios, we focused on two specific cases, starting with the analysis of spectra with poor usable bandwidth. This approach allows us to identify and discard extremely noisy signals from THz images, ensuring that only spectra with a good SNR in the frequency range of interest are analyzed. The second case involves analyzing spectra that contain mercury sulfide (HgS), also known as vermilion, a reddish pigment with historical and artistic relevance. Particularly, this pigment exhibits a spectral fingerprint at 1.14 THz, which will help us to validate the accuracy of the method. The results of this analysis are shown in Fig. 3.6 using a smoothing width $w_s = 6\%$ and $n = 3$.

Spectra corresponding to the first case of interest are shown in Fig. 3.6 a) - c), where it is easy to note that these signals are extremely noisy. In this case, the algorithm calculates ω_c between 0.51 THz and 0.71 THz, which we would consider as spectra with a limited usable bandwidth for our analysis, taking into account the absorption peak of vermilion at 1.14 THz.

For the second set of signals of interest, Fig. 3.6 d)–f) shows spectra of measurements where vermilion was present. Although the absorption peak is easily distinguishable, the algorithm correctly calculates the cutoff frequency in d) and f). However, in e), the cutoff frequency appears to be incorrectly located at a higher frequency, as the spectral amplitude clearly decays to the noise floor before reaching 2.2 THz. To correct the cutoff frequency in this spectrum, the value of w_s was increased to 9%, resulting in $\omega_c = 1.5$ THz.

From these results, we can establish a technique that automates the estimation of the cutoff frequency in large volumes of spectra, such as

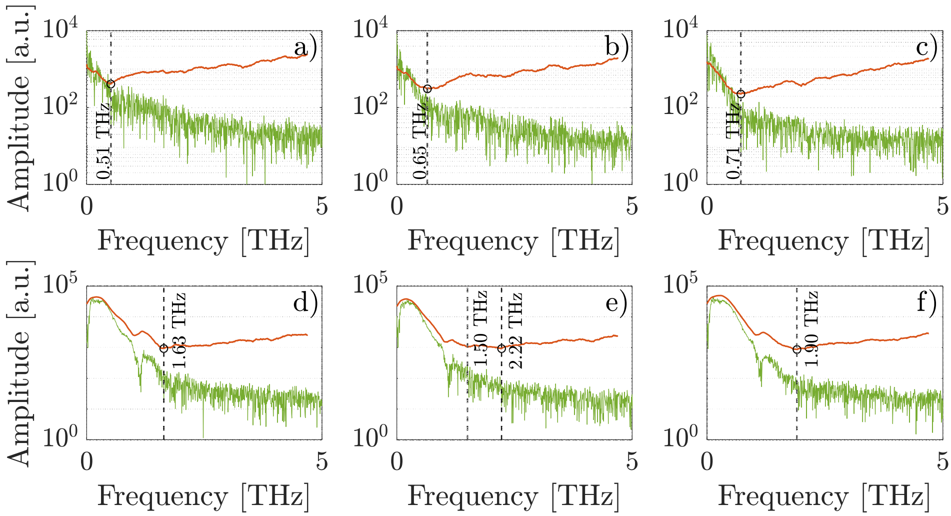

Figure 3.6: a)-c) Spectra corresponding to extremely noisy signals.d)-e) Spectras corresponding to a vermilion sample. The red solid lines represent the product $n^3G(\omega)$, which generates a minimum indicated by the vertical dashed black lines

those in a THz image. In the next chapter, we will demonstrate the direct application of the algorithm for calculating ω_c on a dataset corresponding to a Russian Icon, which enabled us to generate an accurate map of vermilion.

Chapter 4

THz-TDI for analyzing CH paintings

When analyzing an artwork using any of the scientific methods mentioned in the first chapter, including terahertz time-domain imaging (THz-TDI), valuable information can be obtained. These studies can reveal significant details about the manufacturing process of the artwork, interventions, restaurations, levels of degradation, or even uncover hidden features within the object. This motivation drove the research presented in my master's thesis, an investigation done on the *icon* titled *Our Lady of Kazan* using THz spectroscopy [65]. In that study, we identified a pigment and analyzed the layer distribution of the artwork by processing THz signals.

Considering new perspectives on stratigraphic and spectral analyses, we decided to analyze two datasets; a painting by Pablo Picasso and the Russian Icon presented in [65]. Additionally, we applied the algorithm for stimating the cutoff frequency introduced in the previous chapter to accurately identify vermillion in the Russian Icon. Futhermore, we present a super-resolution stratrigraphy method to analyze layer distributions in a non-destructive and non-invasive way. We will take the oportunity to analyze the existing data from the icon again, as it is a particularly interesting object in terms of the materials used in its construction, its stratigraphic distribution, and the deformation of its wooden support. With these considerations, this chapter focuses on the processing of frequency and time-domain signals from the THz images of the aforementioned artworks.

4.1. Analyzing an icon: Time-of-flight and Peak-to-Peak image

As explained in Chapter 2, since THz-TDS allows the emission and recording of a single-cycle THz pulse, the technique is a powerful tool for studying stratigraphy and topography, analysis done in the time-domain. In addition, the information obtained from analyzing THz signal in the time-domain can be relevant for assessing the conservation and deterioration states of the artwork. To provide the reader with an appropiate perspective on the usefulness and practicality of analyzing an artistic object by THz-TDI, we will first present two simple imaging techniques: the *time-of-flight* and the *peak-to-peak* imaging. These techniques will be applied to the surface analysis of the icon.

An *icon* is a religious artefact usually found in the Orthodox Church, portraying relevant biblical characters. Because of its religious importance, gold or even silver is often included as part of the materials used in icons [66]. Additionally, icons are built on a wooden tablet, followed by a preparation layer, layers of paint and varnish [67], making this type of artifact highly interesting for analysis by THz-TDI.

In our case, we will analyze a Russian Orthodox icon, a reproduction of *Our Lady of Kazan* by an unknown artist, shown in Fig. 4.1. The entire artwork was scanned as a part of Emanuele d'Angelo's master's project in 2017 [68], under the supervision of Dr. Peter Uhd Jepsen and Dr. Falko Kuesker. In summary, the icon was painted on a 21.5 × 27 cm wooden

Figure 4.1: Photography of *Our Lady of Kazan* by an unknown artist. Profiles: a) upper, b) front and c) bottom.

tablet, portraiting a bust of the Virgin Mary wearing a golden robe with blue details and carrying the infant Jesus. In addition, from the study done in [68], it is known that gold leaf was applied to cover the background of the wooden tablet. Also, gold painting was applied as details on clothing of both characters. Mercury sulfide (HgS, also known as vermilion) is also present in the artwork. Moreover, from a visual inspection, as Fig. 4.1 a) and c) show, the wooden tablet exhibits a concave deformation.

We will start by analyzing the time-of-flight (ToF), which is useful for a detailed examination of the spatial distribution of an interface by analyzing the pixel-by-pixel time delay of a specific echo from the THz image. For example, if we calculate the time delay of the first interface, the ToF will correspond to the surface of the sample, as shown in Fig. 4.2. As expected, the ToF of the icon revealed the concave deformation in the wooden tablet, as shown in Fig. 4.1 a) and c), corresponding to the upper and bottom profiles of the icon. From ToF data, we calcuted that the icon exhibits a maximum deformation of approximately 3.3 mm between the bottom left corner and the center of the artwork. We also observed some small reliefs on the surface of the faces and necks of the Virgin and the child, in addition to the details on the clothing.

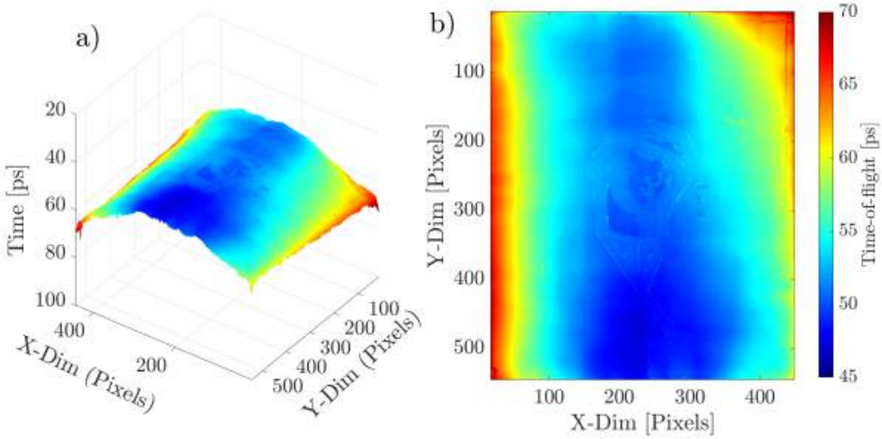

Figure 4.2: ToF image of the icon in a) 3D and (b) 2D, showing the time delay of the first reflection. The concave shape of the artwork is easy to notice in a), while the relief details on the face, neck, and clothing are clearly visible in b)

On the other hand, the peak-to-peak image is obtained by calculating the difference between the maximum and minimum amplitudes on a THz trace. Tipycally, this difference corresponds to the the first reflection of the measurement. This method provides an indirect but practical way to measure the attenuation of the reflected THz beam at the surface. The resulting image can help to identify metallic areas (highly reflective), zones with some kind of degradation, or even previous interventions. Fig. 4.3

shows the peak-to-peak image of the icon compared with the visible image.

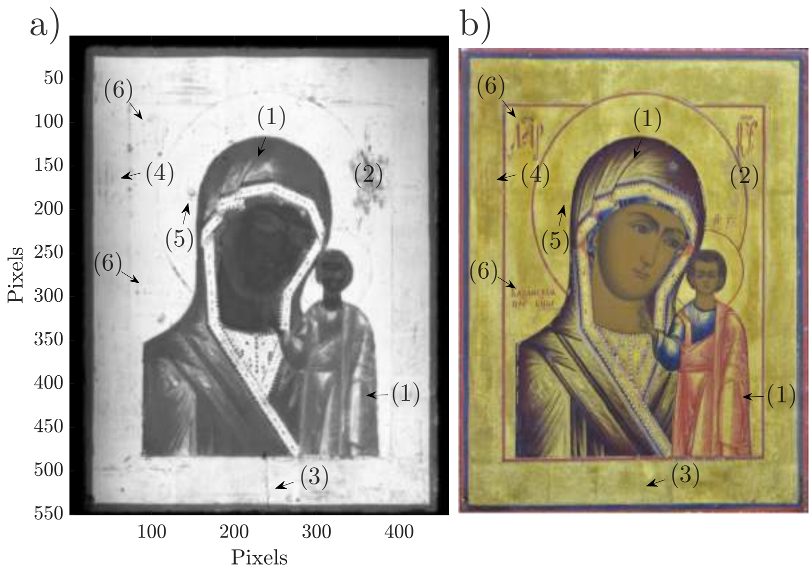

Figure 4.3: a) Peak-to-peak image of the first echo recorded compared with its visible image, shown in b).

As we can see from Fig. 4.3 a), it is easy to identify the strong reflection from the gold leaf applied in the background, shown as white in the color scale. Fig. 4.3 a) also highlights the extraordinary artistic skill of the artist, as the characters were painted with extreme precision in areas where the gold leaf had to be removed. The peak-to-peak image confirms the use of metallic paint on the clothing, as indicated by two areas labeled (1), where the golden details now appeared as white.

Additionally, the peak-to-peak image reveals details about the state of conservation, such as previous restoration work on the left side of the Virgin's head, indicated by (2), which appears as a large dark area against the strong reflection of the background. A significant crack in the lower part of the painting, labeled (3), as well as scratches and small areas where the gold leaf has detached, labeled (4) and (5) respectively, appear as small dark spots throughout the icon. Moreover, a close visual inspection shows clear evidence that the red frame, halos, and inscriptions were painted over the gilding, as these areas exhibit a very low contrast in Fig. 4.3 a). This is particularly noticeable in (6), where the red inscriptions are barely visible.

4.2. Vermilion identification

From the investigation done in [68], a set of X-ray fluorescence measurements revealed the presence of Mercury Sulfide (HgS), also known as vermilion, as indicated in Fig. 4.4. This pigment has been extensively used across various cultures throughout history due to its suitable properties for painting, including good adhesion, vibrant color, and low hardness, which make it easy to grind [69].

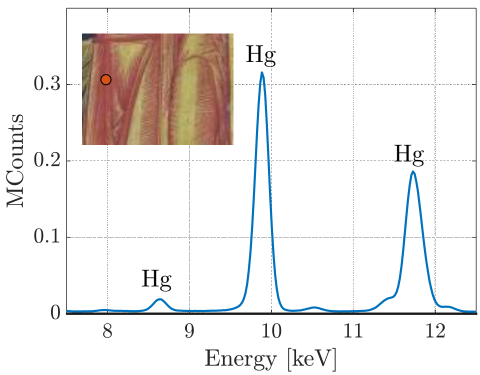

Figure 4.4: XRF spectrum measurement from the area of the child's clothing, indicating the presence of mercury.

Given the historical importance of vermilion, some researchers have focused their investigations on understanding the degradation process of this pigment, such as darkening, using optical techniques [70, 71]. These studies provide new perspectives on understanding how pigments changes the quality of a paiting over time. Considering the importance of analyzing pigments, in the last chapter we will introduce a serie of measurements to explore the investigation of certain pigments by multiphoton absorption and emission of light, also known as *multi photon excited fluorescence*. Vermilion is also an interesting pigment for THz investigation, as it exhibits absorption at THz frequencies, specifically at 1.14 THz. This absorption process is caused by the translational motions of Hg and S atoms [72].

As part of the work done in [65], we developed an algorithm for detecting vermilion in the THz image of the icon by identifying its characteristic absorption peak and locating pixels where the vermilion was applied. However, the algorithm also detected the pigment in pixels where the background noise extended to 1.14 THz, leading to misidentification of vermilion. In other words, the algorithm also detected random noise oscilations instead of the absortion peak from the pigment.

To address this problem, we applied the algorithm for determining usable bandwidth presented in the previous chapter. This analysis will allow us to discard pixels where noise extends below 1.14 THz. By ensuring that only spectra with a good SNR in the frequency range where the absorption band of vermilion is present,are analyzed, we achieve more accurate results.

4.2.1. Mercury Sulfide (HgS) Distribution Mapping

The complete scanned THz image of the icon was analyzed to identify waveforms where vermilion is present, including the calculation of ω_c.

Since the icon does not have a completely flat surface, we decided to use w_s to 12% in the smoothing. This adjustment allowed us to discard pixels corresponding to areas of the icon that are out of the focal plane of the system. Additionally, we decided to only analyze spectra with $\omega_c \geq 1.45$ THz to ensure that the frequency range of our interest is free from noise.

To show the potential of the proposed method, Fig. 4.5 shows the results of vermilion identification before and after applying the ω_c calculation algorithm. Red pixels indicate points where the characteristic peak of the

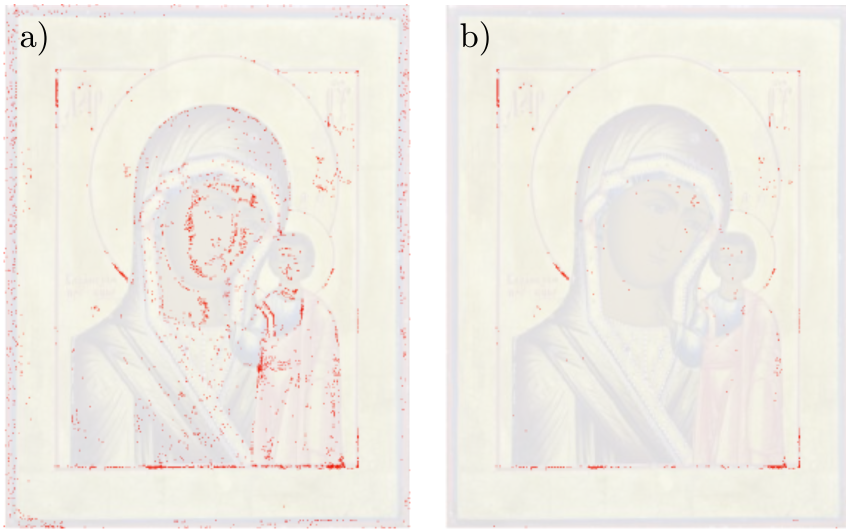

Figure 4.5: Vermilion map a) before and b) after applying the algoritm for ω_c calculation

pigment was detected. The algorithm for vermilion detection, as described in [65], was applied to the complete THz image dataset of the icon between 1.01 THz and 1.27 THz.

As seen in Fig. 4.5 a), which shows the result without considering the calculation of ω_c, vermilion was detected in pixels corresponding to the outer frames of the icon and the face of the Virgin, despite no evidence of the vermilion spectrum in these areas. This misidentification is due to noise in the THz spectra.

In contrast, in Fig. 4.5 b), where the ω_c calculation algorithm was applied, we can clearly observe clustered areas with red pixels. Moreover, the algorithm has effectively reduced the presence of vermilion in pixels corresponding to the frames and the face of the Virgin, removing 84% of erroneously detected vermilion-positive pixels from the ω_c calculation. This demonstrates the effectiveness of the ω_c calculation algorithm in reducing false positives and improving the accuracy of vermilion detection in THz imaging.

Although Fig. 4.5 b) clearly identifies areas where the vermilion absorption peak was detected, it is important to consider the discarded pixels as waveforms where the vermilion absorption peak is likely present, but the noise did not allow an objective detection of the characteristic peak. This approach was considered because, despite Fig. 4.5 b) shows no vermilion-positive pixels in the clothing of the child, this pigment was detected in that area by the XRF analysis, as shown in Fig. 4.4. Considering this approach, Fig. 4.6 a) shows a vermilion detection map where the red pixels indicate areas with clear detection of the vermilion absorption peak, and blue pixels represent areas where the presence of vermilion is probable but inconclusive due to noise.

As seen in Fig. 4.6, a total of six zones with clustered red pixels were detected. These zones correspond to areas painted with a reddish pigment in the icon, as shown in Fig. 4.6 b). Furthermore, a direct observation confirmed the absorption peak of vermilion, as shown by the spectra in Figs. 4.6 c)-d).

Based on the results from this analysis using THz-TDI, it is notable that vermilion was identified only in specific areas, particularly in parts of the halos and frames of the icon, as shown in Fig. 4.6 a). From this analysis, it can be inferred that these areas correspond to retouches made during some stage of restoration or intervention on the artwork. Futhermore, given that there are no visible differences between the mercury sulfide-based pigment and the reddish pigment used in the rest of the icon, this analysis is particularly signficant since THz-TDI allowed us to differentiate between the two red pigments used in the work.

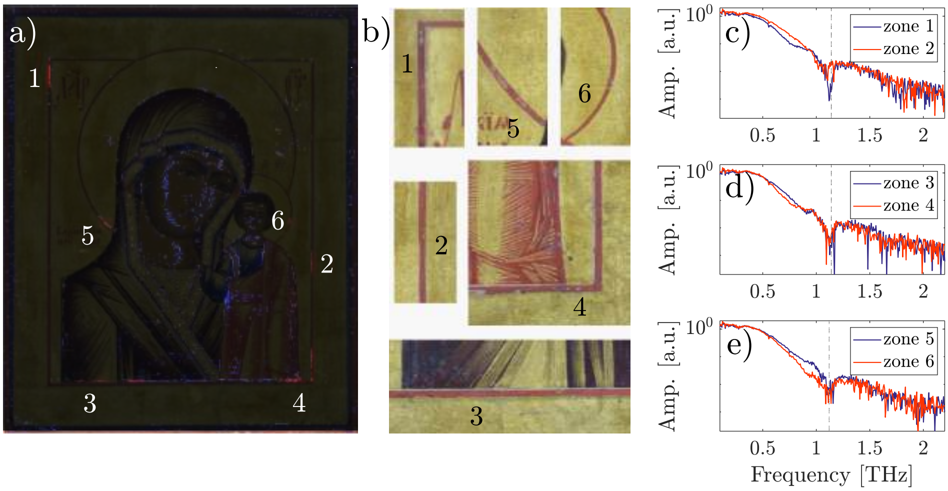

Figure 4.6: a) Vermilion detected in the icon; we identified six areas where the vermilion spectrum was detected. b) Visual photographs of the 6 zones in a), painted with a reddish pigment. c-e) Spectra of waveforms corresponding to the six zones enumerated in a), with the absorption band at 1.14 THz, indicated by the dashed vertical line.

4.3. Stratigraphic analysis

As mentioned in Chapter 2, a significant advantage of THz-TDI in conservation science is its ability of analyze stratigraphy non-invasively. In principle, this type of analysis could be performed without the need for post-processing of the recorded signals; however, an important aspect to consider when studying the stratigraphy using raw data is the potential for inaccuracies.

Suppose we analyze a paint layer with a refractive index $n = 1.5$ in the THz range. If the THz pulse used has a Full Width at Half Maximum (FWHM) of 0.45 ps with a Gaussian profile, the minimum paint layer thickness required to distinguish between the two reflections at each interface is approximately 45 μm. If the layer is thinner, it becomes challenging to correctly identify the two reflected echoes. In other words, if the layers are optically thick compared to the wavelengths within the THz spectrum, it is possible to perform a proper stratigraphic analysis without post-processing. However, in practice, echoes often overlap partially or completely.

In this scenario, it is highly recommended to apply processing to temporally separate the overlapping pulses. As introduced in Charper 2, the reflected THz signal from a multilayered sample is the convolution of the incoming THz pulse with the impulse response function, ideally consisting of a series of ideal impulses corresponding to each interface of the sample. The most common technique to retrieve the impulse response funtion for performing accurate stratigraphic analysis is deconvolution. Basically, conventional deconvolution involves applying the inverse Fourier transform of the transfer function, which is the ratio of the reflected THz spectra to the reference THz spectra. Additionally, spectral filtering can be applied to enhance the results [73].Another increasingly used technique in recent years for studying stratigraphy in THz-TDI is *sparse deconvolution*, categorized as a high-resolution technique.

4.3.1. Sparse Deconvolution

As with conventional deconvolution, sparse deconvolution aims to recover the impulse response function from a THz reflected signal of a multilayered sample. However, sparse deconvolution is characterized by explotting the sparsity of a signal, i.e., that has few non-zero elements. Unlike conventional deconvolution, sparse deconvolution operates in the time-domain. Mathematically, sparse deconvolution is expressed as follows.

The THz reflected signal in the time domain $y(t)$, can be expressed as a convolution of the incident THz pulse $h(t)$ with the impulse response function $f(t)$, which corresponds to the structute of the sample [74]

$$y(t) = h(t) \otimes f(t) = \int h(\tau) f(t-\tau) d\tau. \tag{4.1}$$

In discrete form, which is our case, we can express Eq. 4.1 as

$$y_n = \sum_{m=0}^{M-1} h_m f_{n-m} + e_n, \tag{4.2}$$

where e_n is noise originated from the system, m and n are the data points indices and M is the length of the data points. Now, we can express Eq. 4.2 as the matrix product

$$\mathbf{y} = \mathbf{Hf} + \mathbf{e}. \tag{4.3}$$

Here, $\mathbf{H}$ contains delay versions of $\mathbf{h}$. The basic idea of sparse deconvolution is to retrieve f by approximating the reference signal $\mathbf{y}$ to $\mathbf{Hf}$, considering that f has few nonzero elements. This problem can be solved by considering Eq. (4.3) as a optimization problem, which, in our case, consist of minimizing a function by choosing values within an allowed set, given by

$$\min_{\mathrm{f}} \frac{1}{2} \parallel \mathbf{Hf} - \mathbf{y} \parallel_2^2 + \lambda \parallel \mathbf{f} \parallel_1, \tag{4.4}$$

where $\parallel x \parallel_n$ is the l_n-norm of x expressed as $\parallel x \parallel_n = \sqrt[n]{\sum_{p=1} |x_p|^n}$ and λ is the regularization parameter with $\lambda > 0$. To solve Eq. (4.4), an iterative shrinkage algorithm was proposed given by

$$\mathbf{f}_{i+1} = S_{\lambda\tau}\left(\mathbf{f}_i - \tau \mathbf{H}^{\mathrm{T}} \left(\mathbf{Hf}_i - \mathbf{y}\right)\right) \tag{4.5}$$

where τ is the iterative step size, following

$$\tau < \frac{2}{\parallel \mathbf{H}^T \mathbf{H} \parallel_2}. \tag{4.6}$$

In this case, the soft thresholding operator $S_{\lambda\tau}$ is defined as

$$S_{\lambda\tau}(f[n]) = \begin{cases} f[n] + \lambda\tau & f[n] \leq -\lambda\tau \\ 0 & |f[n]| < \lambda\tau \\ f[n] - \lambda\tau & f[n] \geq \lambda\tau \end{cases} \tag{4.7}$$

In practice, τ is chosen as $\tau = \frac{1}{\|\mathbf{H}^T\mathbf{H}\|_2}$. However, λ and the number of iterations i have to be carefully chosen to correctly calculate $\mathbf{f}$.

To show the potential of sparse deconvolution in stratigraphy analysis, we present the following numerical simulation. We use a Gaussian monopulse with a FWHM of 1.5 ps as reference, with a temporal resolution of 0.1 ps. In this example, we analyze a system with 3 interfaces, simulating 2 layers. The first layer has a fixed temporal thickness of 10 ps. For the second layer, we examine four different thickness: 1.5 ps, 1 ps, 0.7 ps and 0.5 ps. In this case, no noise was added to the signals. We used $\lambda \approx 3\sigma \parallel \mathbf{h} \parallel_2$ as described in [75], with 2000 iterations. The results are shown in Fig. 4.7.

As we can see in Fig. 4.7, the first interface is correctly recovered in the four cases. The second and third interface are also recovered in a) and b). In c), although the last two interfaces are recovered, their amplitude is not correctly retrieved. In scenario d), where we illustrated an extreme scenario where reflections are nearly completely overlapped, sparse deconvolution identifies them as a single reflection.

Now, to explore the effect of noise in the processing, we now focus on analyzing scenario b) from Fig. 4.7, where the second layer has a temporal thickness of 1 ps. We will add different levels of white Gaussian noise, specifically, the signals will have a SNR of 10, 5, 1 and 0.5. The results are shown in Fig. 4.8.

As we can see from Fig. 4.8, the first two echoes at 0 ps and 10 ps are correctly recovered in all cases, regardless of the noise level. However, only the signal with an SNR of 10 recovered the last echo at 11 ps. For the other signals analyzed, additional echoes at 9 ps, 10.9 ps and 11.1 ps appeared.

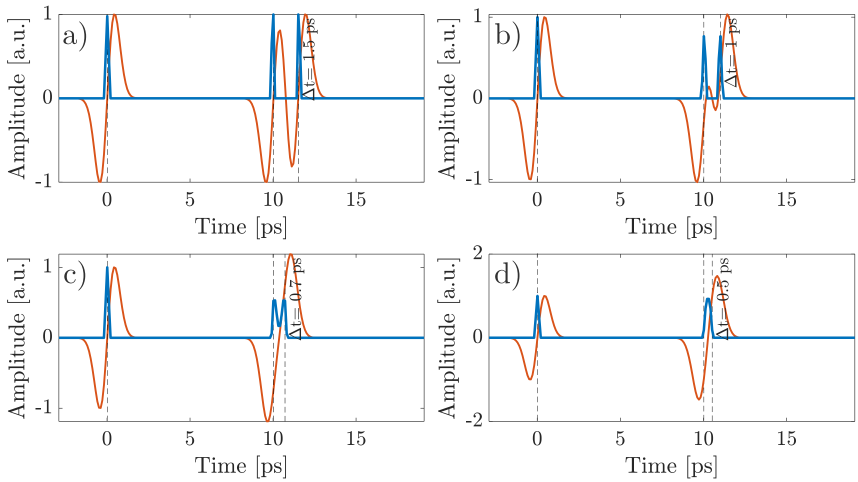

Figure 4.7: Sparsly deconvolved signal from a two-layer system. Orange plots indicate reflected echoes and blue plots indicate the recovered impulse response function. Vertical dashed lines indicate each interface positions. Δt indicates the temporal thickness of the second layer.

This behavior is related to random oscilations of the amplitude and the soft thresholding operation. As shown in Eq. (4.7), soft thresholding operates with the amplitude, making it very susceptible to noise. In this scenarios, is recommendable to adjust the value of λ or even increase the number of iterations.

4.3.2. Sparse deconvolution applied to the analysis in paintings.

Now, we will present two cases of study, where sparse deconvolution is applied to analyze the stratigraphy. The first case correspond to the "Homme au chapeau" by Pablo Picasso [57], introduced as an example in Chapter 2. The THz image, consisting of 360 $\times$ 360 pixels and 800 datapoints in time-domiain with a resolution of $\sim$ 0.1 ps, was provided

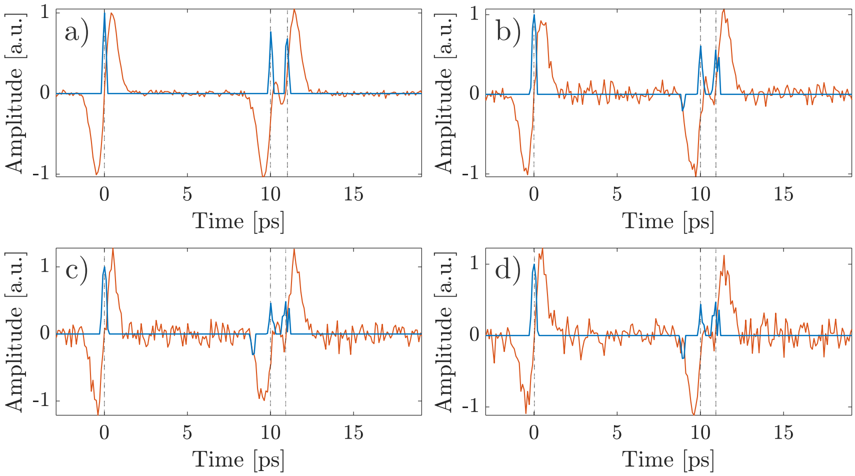

Figure 4.8: Sparsly deconvolved signals from a system of two layers with a SNR of a) 10, b) 5, c) 1 and d) 0.5. Orange plots represent the reflected train echos with noise and blue plots are the recovered impulse response function **f**. Vertical dashed lines indicates the temporal position of each interface

directly by Dr. Kaory Fukunaga. Fig. 4.9 a) shows a visible image of the painting and the peak-to-peak image of the scanned area is shown in b). Some sections of the painting have a smooth surface with a thin layer of paint, in contrast to other areas, such as the background. As explained in [57], the original canvas was glued in a new thick canvas, making this data set an interesting case to study the stratigraphy.

To analyze the stratigraphy of the painting, we processed a b-scan along the X-axis, corresponding to the pixels 210, as incidated by the dashed line in Fig. 4.9 b). The complete b-scan was processed with sparse deconvolution, using 5000 iterations, with $\tau = \frac{1}{\|\mathbf{H}^T\mathbf{H}\|_2}$ and $\lambda = 0.75$. The raw b-scan and the sparsly deconvolved signals are shown in Fig. 4.10 a) and b), respectively.

In Fig. 4.10, positive and negative peaks are represented as red and blue, respectively. In case of b), which corresponds to the sparse decon-

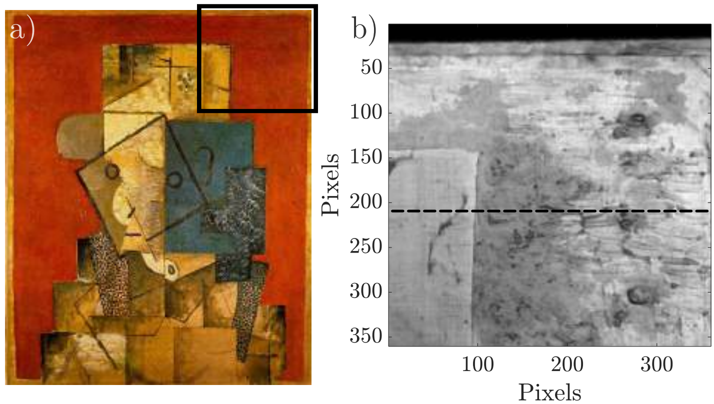

Figure 4.9: a) "Homme au chapeau" by Pablo Picasso, oil painting on canvas [57]. The black square corresponds to the area scanned by the THz system. b) Peak-to-peak image from the raw THz data.

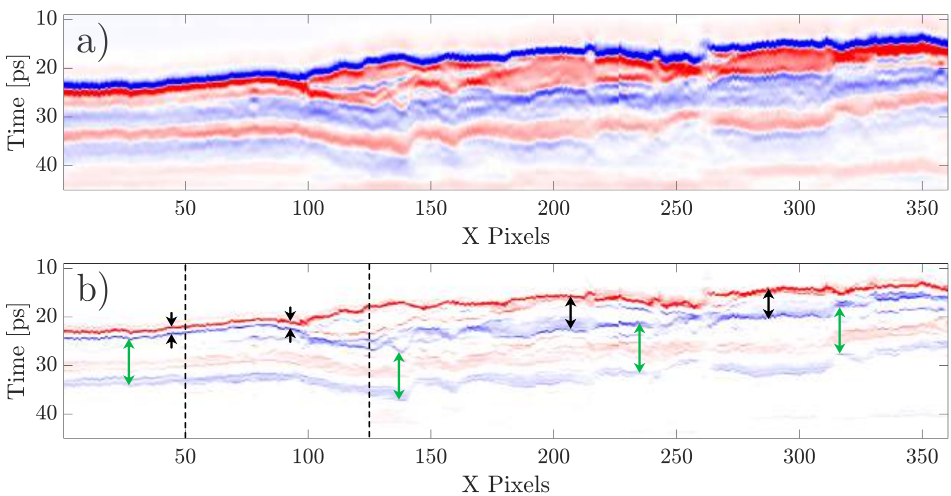

Figure 4.10: B-scans from the Y-Pixels 210, a) raw and b) sparse deconvolved. Positive peaks are shown in red and negative peaks are shown in blue.

volved b-scan, it is easier to analyze the stratigraphic distribution of the painting, as the interfaces found in the inner structure are cearly indicated by positive or negative peaks. Additionally, it is possible to identify the original canvas and the canvas on which it was glued, as the thickness of the new canvas remains constant, as indicated by the green arrows in Fig. 4.10 b). Moreover, as previously mentioned, the original canvas, indicated by the black arrows, exhibits variations on its thickness, which are clearly observable before and after X-pixel 100. To compare these thickness changes,Fig. 4.11 shows the waveforms from the pixels 50 and 126, as indicated by the dashed lines on the b-scan.

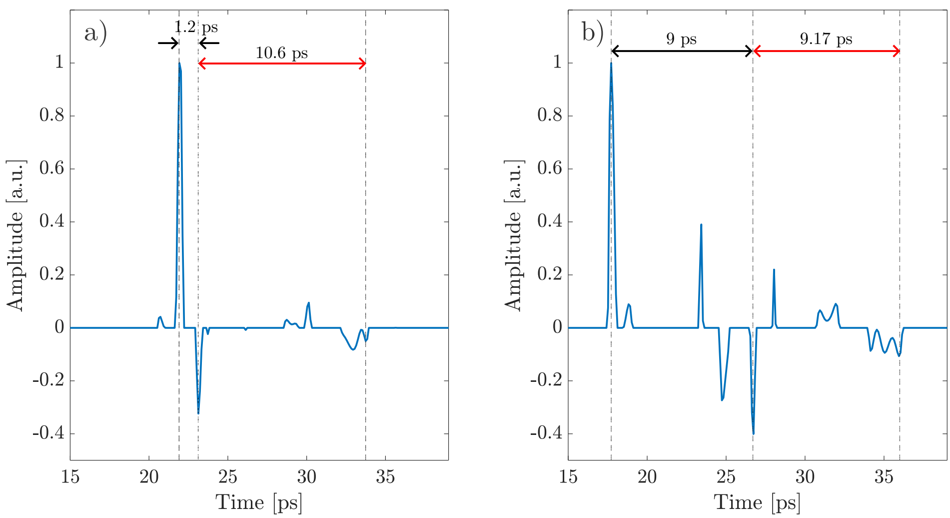

Figure 4.11: Waveforms showing the change of thickness in the original canvas. Signals corresponding to pixels a) 50 and b) 126 of the sparse deconvolved b-scan.

In Fig. 4.11, the layer corresponding to the original canvas are indicated by black arrows, and the new canvas is indicated by red arrows. The change in thickness of the original canvas is obvious, from 1.2 ps in a), to 9 ps in b). If we assume a mean refractive index of 1.5, the thickness changes from 120 μm to 900 μm. As for the new canvas, the variation in thickness from 10.6 ps to 9.17 ps is probably due to an inhomogeneous application of the preparation layers on the canvas itself. Additionally, we can observe at least three interfaces within the original canvas in b).

The second case of interest is the Russian icon. In this case, since the icon exhibit a concave deformation, we decided to analyze only b-scans along the Y axis, where the wooden tablet remains relatively constant. For sparse deconvolution, we achieved satisfactory results with 5000 iterations, using $\lambda = 0.0047$ and τ calculated similarly to the previous analysis. In Fig. 4.12 we present the deconvolved b-scans, corresponding to the X-pixels 236 and 320, which include the faces and clothing of the Virgin and the child, respectively.

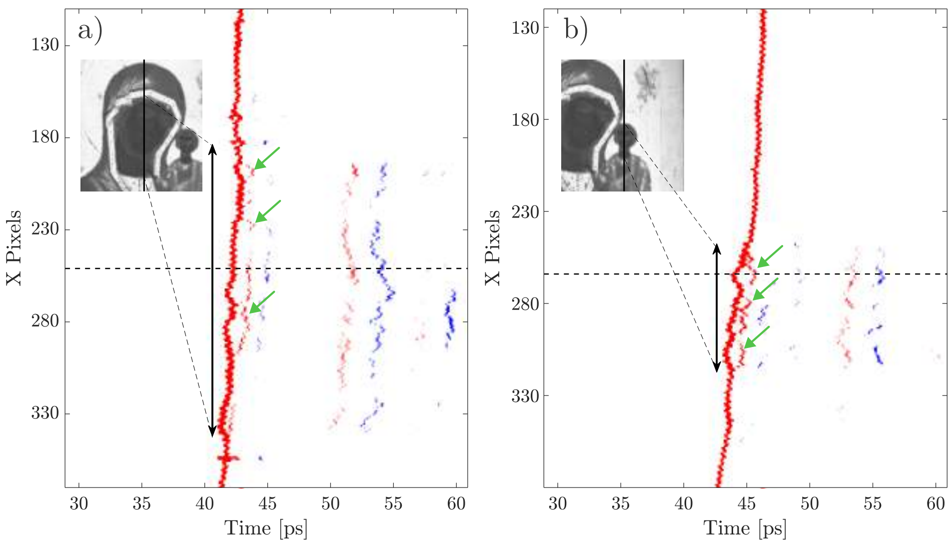

Figure 4.12: Sparse deconvolved b-scans corresponding to the areas of the faces of the Virgin and Child are shown in a) for X-pixel 236 and b) for X-pixel 320. Vertical lines in the insets indicate the areas where b-scans were extracted.

As shown in Fig. 4.12 a) and b), the b-scans reveal a multilayer structure only in the areas indicated by the black arrows,whereas outside these regions, the gilding reflects the THz radiation. Additionally, an extra interface was identified in the areas corresponding to the face and neck of the characters, indicated by green arrows in the b-scans. Furthermore, Fig. 4.13 a) and b) shows the waveforms corresponding to the pixels Y = 251 and 264, respectively, where up to seven interfaces or six layers were identified. The interface labeled as "I2", indicated by green arrows, corresponds to the additional interface found in the b-scans. This finding is consistent with our observations in the ToF image, Fig. 4.2 b), where it is possible to distinguish reliefs on the areas of the face and neck of the characters, areas where interface I2 was identified.

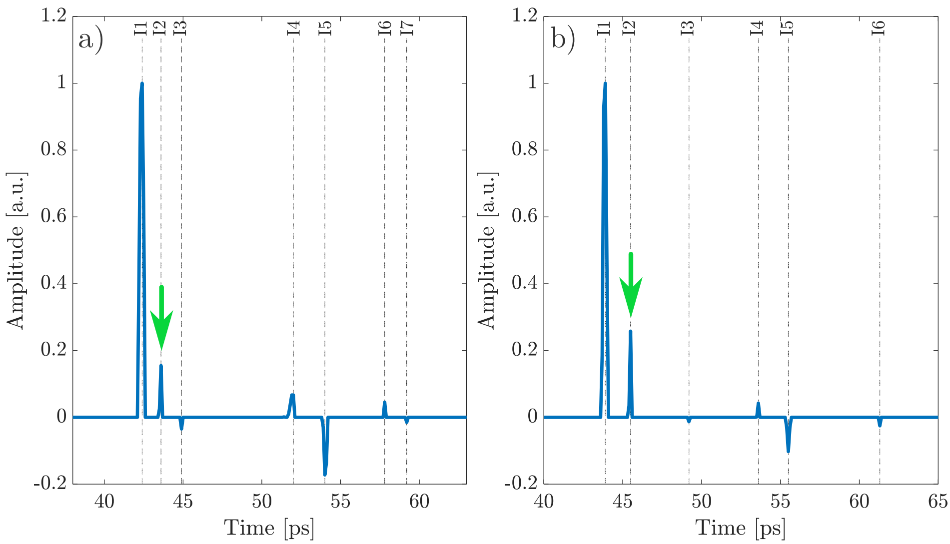

Figure 4.13: Processed waveforms corresponding to pixels a) 251 and b) 264 from the b-scans. Interface labeled "I2" and indicated by the green arrows, is only present in areas corresponding to faces and necks.

We have to mention that the analysis done in this chapter, the calculation of the cutoff frequency ω_c and the analysis performed to the Russian icon were published in [76] and [77], respectively.

4.4. Limitations of THz-TDI

As we have shown in this chapter, THz-TDI offers a safe method for analyzing artistic objects, such as the paintings previously presented, as provides detailed insights into their internal structure and composition. However, the use of lenses to focus the THz beam implies a significant limitation that must be considered. Only signals reflected from the surface at the focal length will show a enough SNR for effective processing and analysis. Out the focal length, the SNR decreases, making complicate to perform a proper data processing. For example, as shown in Fig. 3.5, the spectrum corresponding to the sample placed at the focal plane shows a ω_c =1.66 THz, decreasing to $\omega_c \approx$1.3 THz at -3 mm out of focal plane, and to $\omega_c \approx$1 THz at -12 mm.

Due to these restrictions, only objects with completely or relatively flat surfaces, such as paintings, buildings, or even sculptures, can be scanned with a traditional THz-TDS system. For objects with complex shapes, the irregular surface does not allow a normal incidence measurement, making rather complicated to analyze this kind of objects. In this scenario, spot measurements instead of b-scan measurements can be made in areas of interest to explore the inner structure. In addition, the incorporation of certain mechanisms such as robotic arms can facilitate measurements at normal incidence, improving the accuracy of the analysis. In the next chapter, we will introduce an alternative technique that enables the scanning of objects with complex shapes.

Chapter 5

3D THz-TDS Synthetic Aperture Radar Imaging

As demonstrated in the previous chapter, THz-TDI offers valuable insights by analyzing the stratigraphy of artistic objects. However, a significant limitation when analyzing cultural heritage artifacts is the shape of the object. THz-TDS uses lenses to focus the THz radiation, but only the THz radiation reflected from the surface at a distance equal to the focal length will exhibit an appropriate cutoff frequency ω_c, typically $\omega_c > 1$ THz. At lower frequencies, the SNR decreases, complicating the interpretation and processing of the signal. This scenario becomes more complicated when we deal with samples with irregular shape, as the reflected THz beam will not reflect at normal incidence, making the task of generating a THz image more complex.

A recently introduced imaging technique using THz radiation offers the ability to generate 3D images in a lensless configuration, allowing for the analysis of objects with irregular surfaces and complex shapes. In this chapter we will present *3-Dimensional THz -TDS Synthetic Aperture Radar Imaging* as an alternative imaging technique for heritage science, focusing on its application in stratigraphic analysis of cultural heritage objects.

This work was conducted during a research stay at the Faculty of Engineering, in the THz Systems Group at the University of Duisburg-Essen, Germany. The laboratory equipment and code used in this analysis were provided by the group led by Prof. Dr. Jan C. Balzer.

5.1. THz -TDS Synthetic Aperture Radar Imaging

Synthetic Aperture Radar (SAR) is a radar-based technique introduced by Carl Wiley in 1951 [78], which has been applied in various fields, including astronomy [79, 80], weather forecasting [81, 82], and defense applications [83, 84]. SAR allows for the reconstructions of high-resolution images by moving the emitter/receiver antenna along a defined path, emitting microwave radiation towards a target, and recording the reflected echoes. The idea behind SAR is to coherently assemble these recorded echoes into a single image with higher resolution compared to conventional radar imaging [85].

THz-TDS SAR imaging follows the same principles as conventional SAR imaging but has the potential to achieve higher resolution images compared to those obtained with microwave radiation. In recent years, the THz community has shown increased interest in applying SAR imaging within the THz range [86, 87, 88]. In this section, we explore the concept of circular synthetic aperture, which has been introduced and detailed in [89, 90, 91] for THz-TDS SAR imaging.

In a circular synthetic aperture, as shown in Fig. 5.1, $\mathbf{E}$ and $\mathbf{D}$ represent the positions of the THz emitter and detector antennas, respectively. Both antennas are oriented towards the center of the circle, where the sample is positioned for scanning. In this analysis, the term $\mathbf{P}_i$ is used to denote the position of the i-th point target. The emitter and detector are moved along the circle with a fixed step size $\Delta\theta$, and a total of n measurements are recorded.

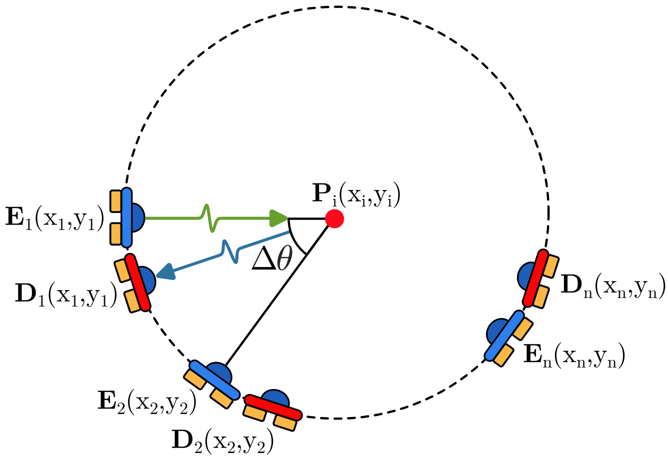

Figure 5.1: Synthetic circular aperture configuration

Since the distance between the emitter and detector remains constant for each measurement, θ_n denotes the position of $\mathbf{E}_n$ and $\mathbf{D}_n$ for the n-th measurement. The recorded signal $s_\mathrm{d}(\theta_n, t)$ is then expressed as

$$s_\mathrm{d}(\theta_n, t) = \sum_i r(\mathbf{P}_i, \theta_n) \cdot s_\mathrm{e}(t - t_{i,n}), \tag{5.1}$$

where $s_\mathrm{e}(t)$ is the emitted THz pulse, $r(\mathbf{P}_i, \theta_n)$ is the reflection coefficient at $\mathbf{P}_i$, and $t_{i,n}$ is the time-of-flight of the THz pulse traveling from $\mathbf{E}$ to $\mathbf{P}_i$ and back to $\mathbf{D}$. Assuming the THz beam travels at the speed of light c_0, $t_{i,n}$ for the n-th measurement is defined as

$$t_{i,n} = \frac{|\mathbf{P}_i - \mathbf{E}_n| + |\mathbf{P}_i - \mathbf{D}_n|}{c_0}. \tag{5.2}$$

This data acquisition allows us to record reflections from the sample at different antenna positions given by n. The set of recorded signals $s_\mathrm{d}(\theta_n, t)$ is called *radargram*. A radargram is a 2D representation of THz reflections from the sample in the time-domain as a function of the antennas positions. An example of an experimental radargram is shown in Fig. 5.2, where the X-axis represents time, the Y-axis indicates the θ_n measurement over the azimuth angle, and the pixel amplitude corresponds to the amplitude of the THz trace recorded at each measurement.

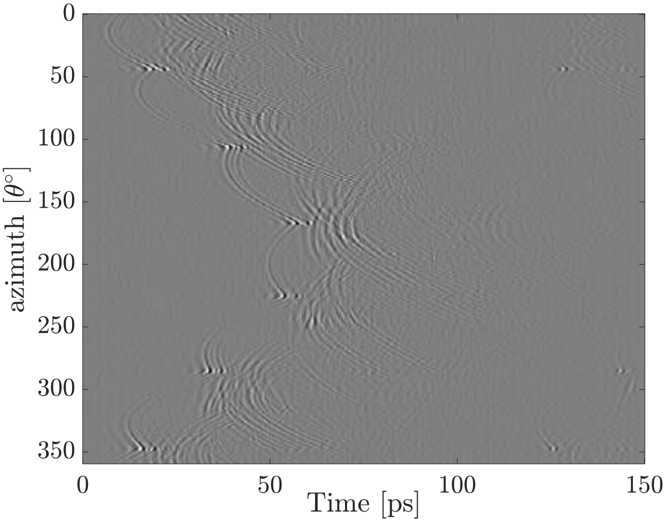

Figure 5.2: Experimental radargram. Multiple reflections can be observed as black and white lines along the azimuthal angle θ

Given that the positions of the antennas in each measurement are known and the time-delay of each echo is recorded in the radargram, image reconstruction becomes possible. The resulting image $I(x, y)$ is recovered by

$$I(x, y) = \sum_n s_\mathrm{d}\left(\theta_n, t - t_{x,y,n}\right) \tag{5.3}$$

where $t - t_{x,y,n}$ represents the time-of-flight from the emitter and detector positions to each pixel in $I(x, y)$ for the n-th measurement. The term $s_d\left(\theta_n, t - t_{x,y,n}\right)$ is referred to as a *subimage*. A subimage is essentially a two-dimensional spatial representation of a single trace contained in the radargram, where the amplitude of the THz trace is assigned to each pixel of the subimage based on the distance traveled by the THz beam. To obtain $I(x, y)$, all subimages are summed.

Since this reconstruction is completely done in the time-domain, it is called *back-projection*. In practice, it is often more convenient to fix the emitter and detector and rotate the sample using a platform. In this case, the technique is called *inverse* circular synthetic aperture.

In a circular synthetic aperture, the resolution will be the same in the x and y directions. When a sample is scanned 360° over the azimuth angle θ, the resolutions is given by [90]

$$\delta_x = \delta_y = \frac{c_0}{2B}, \tag{5.4}$$

where B is the frequency bandwidth of the system. As indicated by Eq. (5.4), the resolution of the image is directly related to the bandwidth; a wider bandwidth results in higher resolution. For commercial systems with a typical bandwidth of $B = 2$ THz, the resolution is $\delta_x = \delta_y = 75\mu$m. In contrast, THz images obtained via raster scanning depend on the step size of the transceiver head on the XY platform, usually resulting in a resolution of 500μm. Compared with conventional THz-TDI, this technique offers an enhencement in resolution.

Taking the same reasoning of the circular synthetic aperture, we can extend the approch to a spherical synthetic aperture, where now a reconstruction over the Z-axis is introduced. In this setup, the sample is scanned not only around the azimuth angle θ but also over the elevation angle ϕ. The resulting radargram, similar in structure to that of the circular synthetic aperture, will stack for each ϕ a set of measurements over θ, as shown in Fig. 5.3. In this radargram, n represents both θ and ϕ, providing the positions of the antennas during each measurement.

We can now express the recorded signal as $s_{\mathrm{d}}(\theta_n, \phi_n, t)$, where θ_n and ϕ_n denote the positions of the emissor and detector at the n-th measurement.

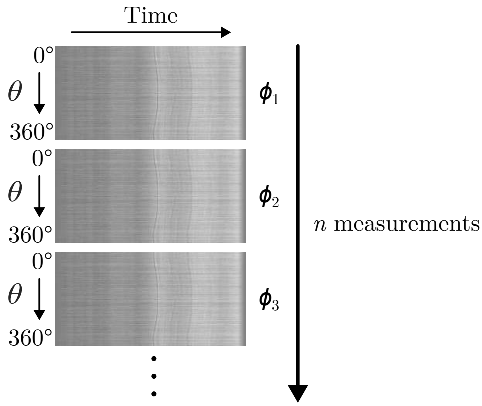

Figure 5.3: Radargram structure for a inverse spherical synthetic aperture

The volume reconstruction of the sample is then given by [91]

$$I(x, y, z) = \sum_{n} s_{\mathrm{d}}\left(\theta_n, \phi_n, t - t_{x,y,z,n}\right). \tag{5.5}$$

.

Due to the symmetry of the spherical configuration, the resolution of the 3D image is consistent with the resolution of the circular synthetic aperture, as described in Eq. 5.4. This applies to δ_x and δ_y, and it extends to δ_z as well.

5.2. Experimental Results

Having theoretically introduced THz-TDS SAR circular and spherical synthetic apertures, we will now discuss the experimental considerations and present the results of analyzing objects of interest. To optimize the 3D image reconstruction, we implemented GPU parallel computing using CUDA with MatLab in the back-projection algorithm.

5.2.1. Data recording

The terahertz system used in this part of the work was a TeraK15 time-domain spectrometer from Menlo Systems. This system consist of a fiber-coupled PCA as, both, emitter and detector, and is pumped with a femtosecond laser pulse at a wavelength of 1560 nm. This system has a speed of aproximately 22 traces per second when the temporal window is 100 ps. For recording the THz radiation over the azimuth θ and elevation ϕ angles, a 3D printed device was used [91]. This device, shown in Fig. 5.4 a), uses two stepper motors to rotate the sample.

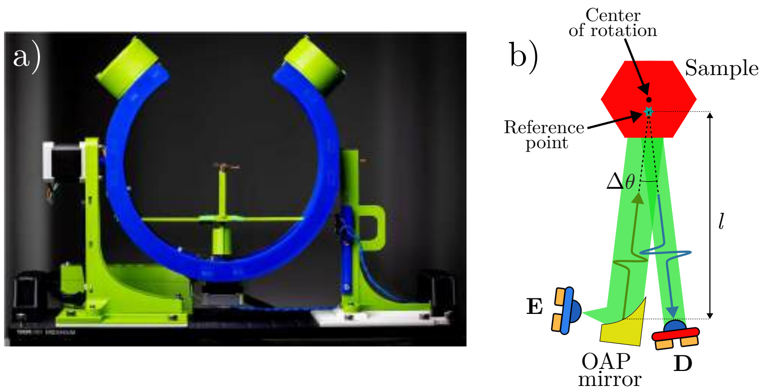

Figure 5.4: a) 3D printed device used for rotate the sample in the inverse spherical synthetic aperture [91]. b) Schematic diagram of the PCAs configuration for recording the radargram of a sample.

Both PCAs, the emitter **E** and the detector **D**, were fixed as shown in Fig. 5.4 b). The angle between the propagation axis of the THz beam $\Delta\theta$ was 24.3° with $l = 16.25$ cm. The THz beam was collimated using an off-axis parabolic (OAP) mirror. A metal post was placed at the center of rotation to record a reference trace. For this purpose, the emitter and detector were aligned to point a reference point on the surface of the metal post, as shown in the illustration. By comparing the time delay between the reference measurement and the sample measurements, the exact positions of the echoes generated by the sample surface can be determined.

5.2.2. Back-projection

To reconstruct the image from the signals stored in the radargram, we -used a back -proyection algorithm. This algoritm sums subimages, with each subimage generated from individual traces recorded in the radargram. The reconstruction process is described by the following equation

$$I(x, y) = \sum_{n} s_{\mathrm{d}}\left(\theta_n, t - t_{x,y,z,n}\right). \tag{5.6}$$

This approach applies to the circular synthetic aperture configuration. Essentially, to construct a subimage, each pixel is assigned the amplitude of a waveform based on the distance d that the THz beam travels from the emitter to the pixel and then to the detector. Given that we used a collimated THz beam, we can approximate the beam as a plane wavefront traveling towards the pixel P, as shown in Fig. 5.5.

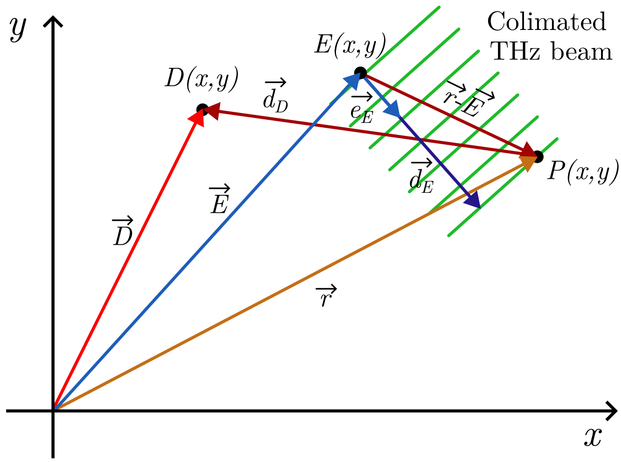

Figure 5.5: Geometry analysis for calculation of subimages. This calculation depends on the positions of the THz emitter, detector and the time-of-flight of each trace.

Therefore, the distance d is given by

$$
\begin{aligned}
d &= \left|\vec{d}_E\right| + \left|\vec{d}_D\right| \\
&= \left|\frac{\vec{e}_E \cdot (\vec{r} - \vec{E})}{|\vec{e}_E|^2}\vec{e}_E\right| + |\vec{D} - \vec{r}| \\
&= \left|\left[\vec{e}_E \cdot (\vec{r} - \vec{E})\right]\vec{e}_E\right| + |\vec{D} - \vec{r}|,
\end{aligned} \tag{5.7}
$$

where $\left|\vec{d}_E\right|$ and $\left|\vec{d}_D\right|$ are the distances traveled by the THz beam from the emitter to the pixel P and from P to the detector respectively. Here, $\vec{E}$, $\vec{D}$ and $\vec{r}$ represent the vector positions of the emitter, detector, and pixel P respectively, while $\vec{e}_E$ is a unit pointing vector indicating the orientation of the emitter.

After calculating d for each pixel, we assign to each pixel the amplitude of the THz trace corresponding to that distance d. An example of a THz subimage generated using this method is shown in Fig. 5.6.

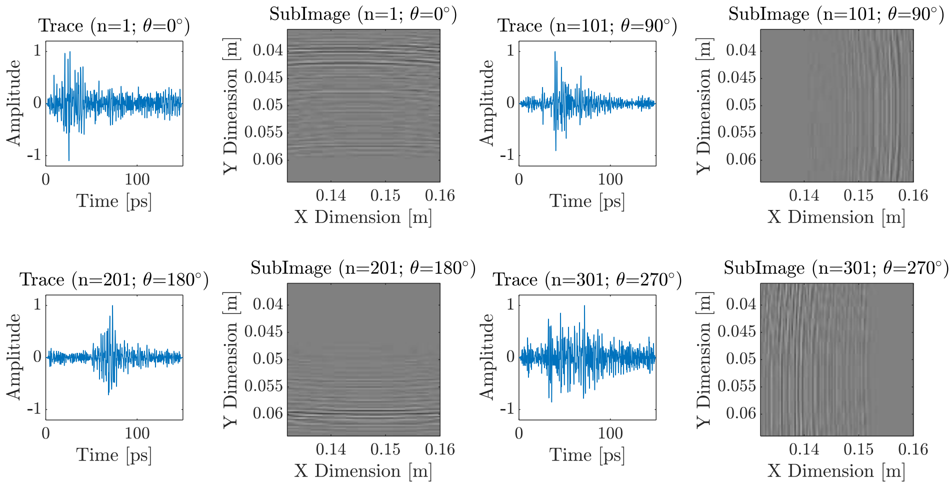

Figure 5.6: Subimages generated using their corresponding traces from the radargram for n=1, 101, 201 and 301, corresponding to θ =0°, 90°, 180° and 270°

In total, the number of subimages will equal the number of measurements stored in the radargram. By summing all these subimages, we will recover the reflections of the interfaces from the scanned sample. The waveforms contained in each subimage will interfere both constructively and destructively, resulting in the reconstructed image. Fig. 5.7 shows a reconstruction of a 20-sided metal die, obtained at an elevation angle of $\phi = 0°$ and an azimuth angle of $\theta = 360°$, resulting in a b-scan in the XY plane.

As shown, at an elevation angle of $\phi = 0°$, only 6 sides of the die are visible in the reconstruction. To achieve a full 3D reconstruction, additional measurements with varying ϕ are required.

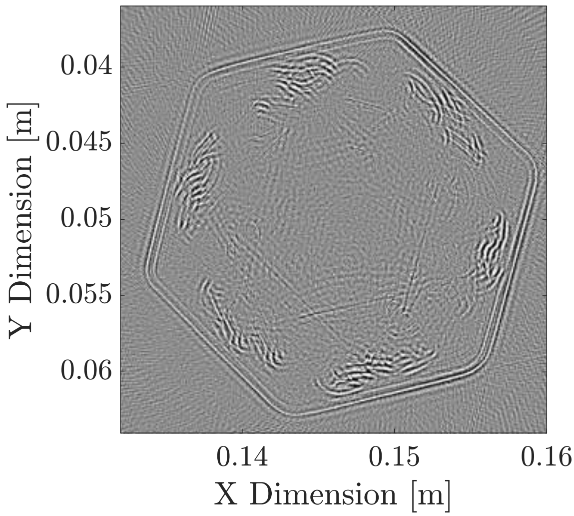

Figure 5.7: B-scan of a 20-sided die in the XY plane obtained by THz-TDS SAR imaging. Only 6 sides are recovered in this b-scan.

5.2.3. Inverse spherical synthetic aperture

Using 3D THz-TDS SAR imaging with an inverse spherical synthetic aperture, we aimed to explore two scenarios; stratigraphy analysis and scanning of an object with an irregular and complex shape. For the first scenario, we decided to follow the same geometry of the synthetic aperture and to 3D print a sphere using PLA filament. The sphere, with a diameter of 35 mm, was initially painted with a primer to ensure proper adhesion of acrylic paint. In total, we painted three areas of interest (AoI) with commercial acrylic paint, leaving a small reference area unpainted. The first AoI was a rectangular layer of silver metallic acrylic paint, typically made with aluminum particles. The second AoI was an arrow painted with green acrylic paint. The final AoI consisted of a red triangle painted over a green square, which was then covered with a yellow circle. Finally, the sphere was entirely painted with blue paint, while preserving the reference area, as shown in Fig. 5.8 a) and b).

For the radargram recording, the azimuth angle θ varied from 0° to 360° in steps of $\Delta\theta = 0.9°$, while the elevation angle ϕ varied from $-72°$ to 40.5° with a step size $\Delta\phi = 0.9°$. This resulted in a total of 50,400 traces. Each measurement had a temporal window of 140 ps with a resolution of 0.033 ps, and each trace in the radargram was averaged over 15 waveforms. Although the direct recording time for the 50,400 traces is approximately 13 hours, when accounting the azimuthal and elevation movements of the platform, along with the file recording time, the total acquisition time increases to over 24 hours.

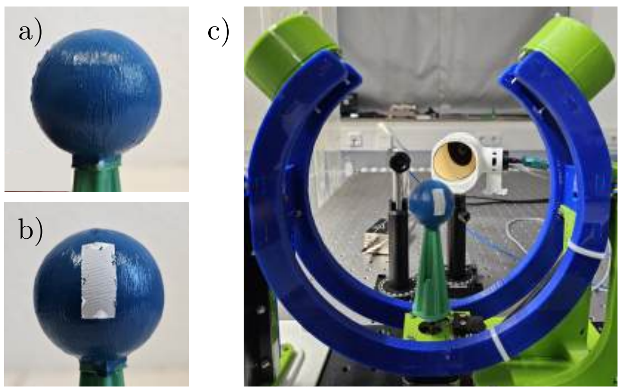

Figure 5.8: 3D printed sample scanning. a) Sample with multiple paint layers. b) Reference area. c) Scanning platform following a inverse spherical synthetic aperture geometry.

To enhance the quality of the reconstructed image, we applied a band-pass filter using Tukey windowing to each recorded trace, filtering frequencies from 0.5 THz to 2.5 THz. This filtering process removes low-frequency components in the time-domain data as well as high-frequency noise. Fig. 5.9 shows the radargram before and after filtering. After filtering the radargram, we applied the back-projection algorithm to reconstruct the object in 3D. The processing was performed on a laptop equipped with 32

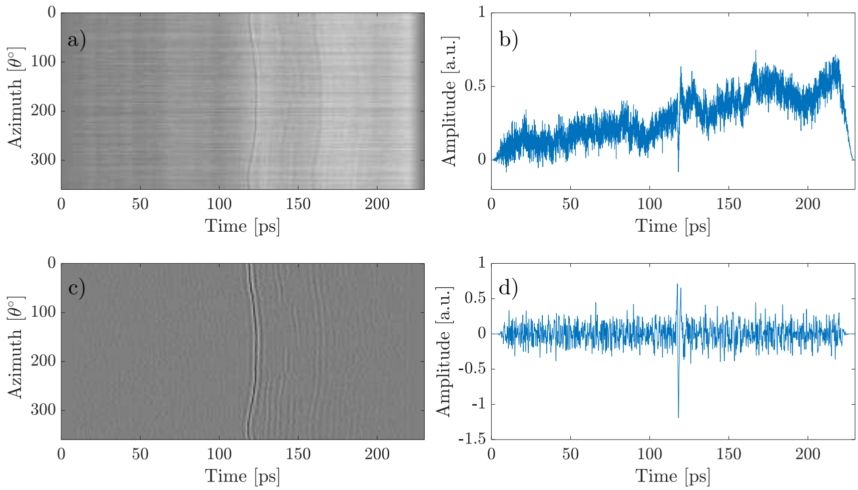

Figure 5.9: Radargram corresponding to $\phi = 0°$, a) before and c) after the spectral filtering. To better show the effect of the filtering, waveforms corresponding to $\theta = 0°$ are shown in b) and d)

GB of RAM, an Intel Core i5-11400H processor, and an NVIDIA GeForce RTX 3050 Ti graphics card. The total processing time was approximately 6 hours. The result, shown in Fig. 5.10, clearly reveals the spherical shape of the sample.

Although the shape of the object was correctly recovered, the amplitude of the echoes reflected from the surface was affected, likely due to errors in the elevation angle ϕ introduced by the stepper motor during the recording stage. This resulted in horizontal fringes with different intensities, as shown in Fig. 5.10 c) and d). By performing an intensity analysis on the data, we were able to identify all the AoI on the sample. The reference area and AoI 1 were the first to be identified, as shown in Fig. 5.11 a).

The reference area is easy to identify, specifically by the sharp edges that appear as fine black lines in the SAR image. Additionally, the AoI 1, where metallic paint was applied, is clearly visible due to its higher amplitude

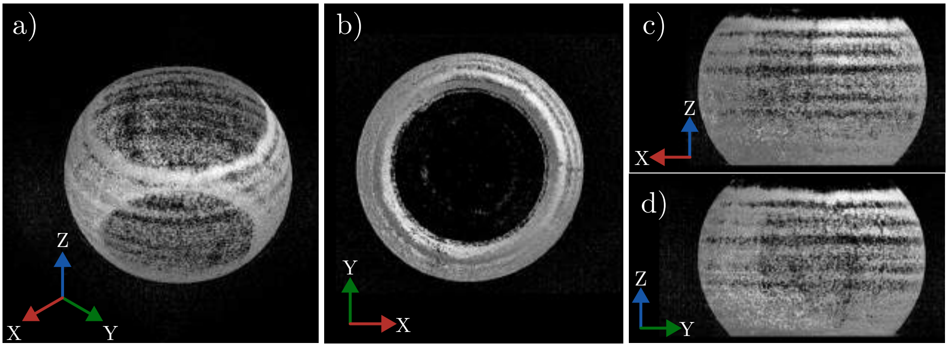

Figure 5.10: a) 3D THz image corresponding to our first sample. b) XY plane view. c) XZ plane view. d) YZ plane view.

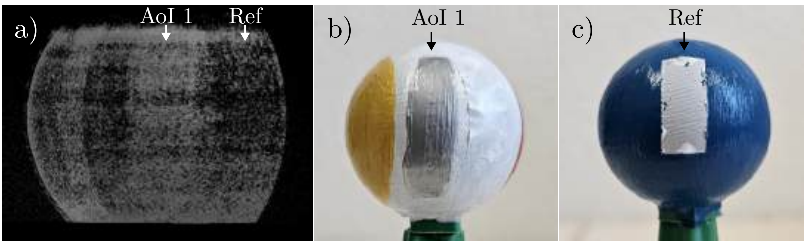

Figure 5.11: a) 3D SAR image of the sample corresponding to the reference area and AoI 1. b) AoI 1 indicated by the arrow where silver metallic paint was applied. c) Reference area where only primer was applied.

compared to other areas.

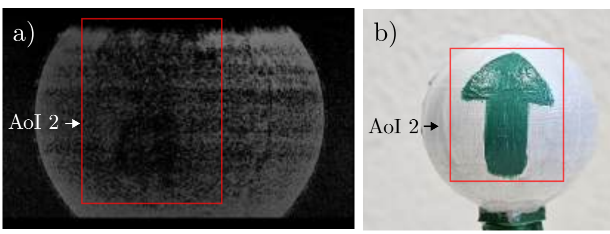

Figure 5.12: a) AoI 2 observed in the SAR image indicated by the red rectangle. b) Green arrow painted on the sample corresponding to the AoI 2.

The AoI 2 is also visible, as shown in Fig. 5.12. However, the tip of the arrow was not recovered because the north pole of the sphere was not fully scanned. In the case of AoI 3, although a clear attenuation in amplitude is observed in this area, as shown in Fig. 5.13, no distinctions were found between the individual figures painted on it.

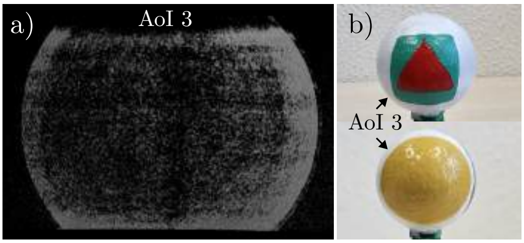

Figure 5.13: a) Area corresponding to the AoI 3. b) Sequence of shapes painted on the sphere corresponding to the AoI 3: first, a green rectangle was painted; next, a red triangle was added; finally, a yellow circle was applied to cover the previous shapes.

In the stratigraphyc analysis, while AoI 1 and 2 were clearly observed and AoI 3 was partially recognized, only two interfaces were identified in the entire SAR image, labeled as I1 and I2 in Fig. 5.14.

This behavior could be due to different factors, including the overlaping of echoes reflected from the paint layers and the high level of noise in each trace in the radargram. It is likely that the two layers observed in the b-scan correspond to the air/paint and paint/PLA interfaces. Moreover, since the sphere was 3D printed, there are air gaps in the inner structure, which were also observed in the b-scans, indicated by black arrows in Fig. 5.14. In the 3D SAR image, these two layers were also identified, as shown in Fig. 5.15, where I1 and I2 are displayed as shells in the surface of the sphere.

The second sample analyzed is a small metallic toy, as shown in Fig. 5.16. Initially, the sample was completely painted. We decided to remove the

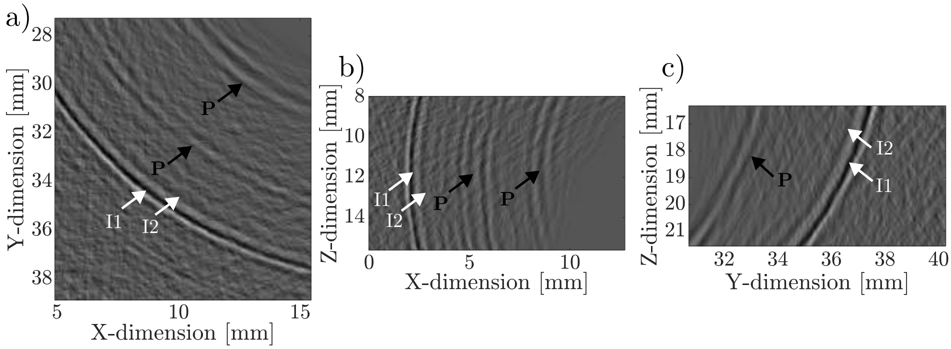

Figure 5.14: B-scans with the stratigraphic distribution of the sphere. Only interfaces I1 and I2 from the paint layers were idenfitied. Additionally, the inner structure of the 3D printed sample is also identified, labeled as P in the b-scans. a) XY plane view. b) XZ plane view. c) YZ plane view.

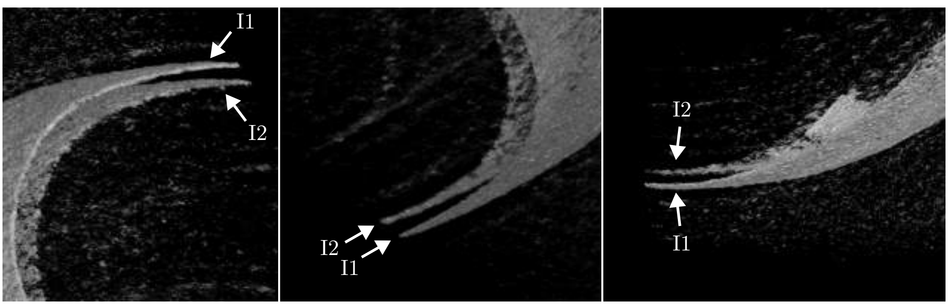

Figure 5.15: Interfaces I1 and I2 idenfitied in different cuts in the 3D SAR image data set.

paint from half of the object with the intention of comparing the areas where the paint layer remains with those where it has been removed. The sample was placed in the scanning station with its head positioned at the center of rotation.

Following the same data processing as with the previous sample, the complete radragram was filtered using a Tukey window from 0.5 THz to 2.5 THz. In the registration of the radargram, the azimuth angle θ varied from

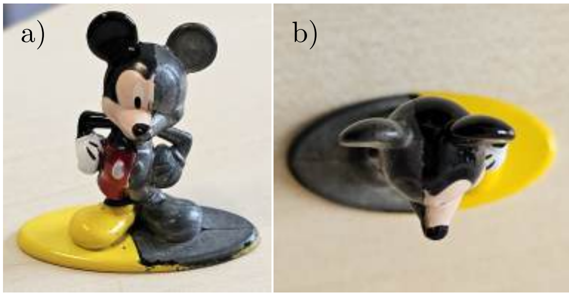

Figure 5.16: Sample two; small metallic toy with complex shape. a) Front view. b) Top view.

$0°$ to $360°$ with a step size of $\Delta\theta = 0.9°$, and the elevation angle ϕ varied from $-72°$ to $84.5°$ with $\Delta\phi = 0.9°$. The radargram contained a total of 69,600 traces, each with a temporal window of 190 ps and a resolution of 0.033 ps. The total recording time for the radargram was approximately 48 hours. Using the same computer specifications as in the first sample, the processing time was around 9 hours. After applying the back-projection algorithm, the 3D SAR image of the second sample is shown in Fig. 5.17

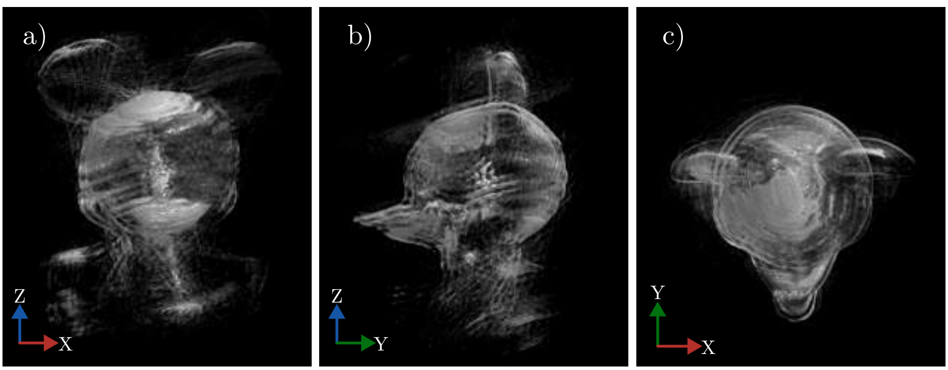

Figure 5.17: 3D SAR image corresponding to the second sample. a) XZ plane view. b) ZY plane view. c) YX plane view.

As shown in Fig. 5.17, the shape of the head is accurately retrieved, including sharp edges like the nose. Other features, such as the ears, are also well recovered, even though these parts have a concave/concave shape. Additionally, part of the right arm and the body are visible in the 3D image. However, since the sample was positioned with the head aligned with the center of rotation on the scanning platform, this section was the only part properly recovered.

One important aspect to consider with this technique is that 3D THz-TDS SAR imaging relies on the constructuve and destrutive interference of each trace contained in a subimage. This implies that the stronger reflections will be preserved in the final result, while weaker reflections are more likely to be attenuated. In objects like this example, with small corners, sharp edges, and concave/convex areas, the THz detector will record multiple reflections not only from the surface facing the detector but also from other parts of the sample. As a result, when the back-projection algorithm is applied, false echoes may be reconstructed due to those additional reflections recorded in the radargram. Due to this consideration, the stratigraphic analysis in this sample was inconclusive.

Although the shape of the sample is correctly reconstructed, more than two interfaces appear in the SAR image. Fig. 5.18 shows a B-scan in the XZ plane, which includes the areas where the paint was removed and where it remains. However, multiple reflections are identified, even in the region where the paint layer was removed. This is a significant observation since the sample has a metallic core, and we expected to detect only one echo in this side of the sample.

In this analysis, we found no distinction between the left and right sides of the sample. We only identified the surface interface as the strongest reflection in the SAR image. Since echoes were also detected within the inner part of the metallic core, we suppose that this misconception is originated

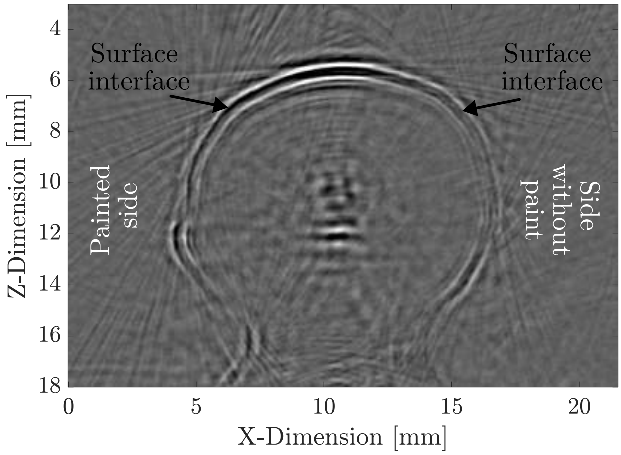

Figure 5.18: B-scan in the XZ plane corresponding to the head of the sample. Multiples reflections are identified, even in the side where the paint was removed

from multiple reflections recorded at different points in the radargram, as described above.

Throughout the whole 3D SAR image, false echoes were consistently identified within the inner part of the sample. In Fig. 5.19 we present three b-scans from different plane cuts. Fig. 5.19 a) shows a b-scan corresponding to the head of the sample in the ZY plane, where it is easy to note the shape of the head and nose. Similarly, in Fig. 5.19 b) and c), which correspond to b-scans in the YX plane at different heights, we observed the same features.

5.3. Future work

As demonstrated in this chapter, 3D THz-TDS SAR imaging offers a viable alternative for generating three-dimensional images using THz radiation, with the notable advantage of being able to analyze objects with complex surfaces. From this initial exploration, which focused on proof of principle of measurements, we can draw some general observations that may

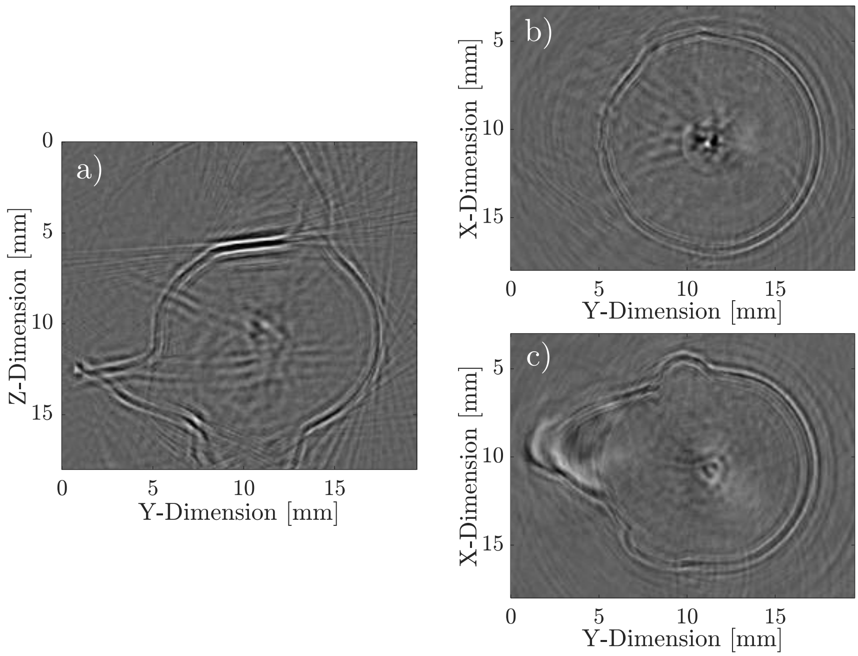

Figure 5.19: B-scans corresponding to the head of the sample showing multiple reflections located in the metal core. a) YZ plane view. b) - c) YX plane view at Z= 7.25 mm and 5.13 mm respectively.

guide the examination of artistic and historical objects in future research.

In general, reflected echoes from optically thin interfaces often overlap, as observed with our first sample. This problem has been addressed in the past through deconvolution techniques [92, 93, 73]. In this context, implementing deconvolution algorithms could be used as an alternative to the bandpass filtering presented in this chapter for processing and reconstructing 3D images. Two potential methods are deconvolution with spectral filtering and sparse deconvolution, as discussed in the previous chapter.

It is also possible to explore edge detection algorithms within the radargram to selectively identify the stronger echoes. This process could help remove multiple reflections that are recovered in the final result, which can introduce misconceptions in the stratigraphic analysis, as seen in our second sample.

One important factor to consider is the noise present in the waveforms. Since 3D THz-TDS SAR imaging is a lensless system, the SNR decreases, leading to increased noise across the whole radargram. To address this, we can apply denoising techniques, such as wavelet denoising, which has been successfully used in THz signal processing [94, 95]. This approach would allow a clearer visualization of the echoes reflected from the interfaces of the object of interest

Finally, the rotation and scanning station can also be improved. Although it works properly for the radargram recording, upgrading to a more stable platform would minimize significant variations when varying the azimuthal and elevation angles.

Chapter 6

Multiphoton and second harmonic studies of pigments

Following our exploration of THz radiation for the evaluation of cultural heritage artifacts, this chapter will briefly discuss our investigation into multiphoton excited fluorescence (MPEF) and second harmonic generation (SHG), specifically aimed at characterizing pigments used in artworks. It is important to mention that this research, done at an early stage in my PhD, is only briefly covered due to a shift in topical focus that occurred over the course of the project. As a result, we will focus on presenting only the most relevant findings.

6.1. Multiphoton Excitation Fluorescence

Fluorescence spectroscopy is one of the most important and widely used techniques for characterizing pigments in art [96, 14, 97, 98, 99]. This phenomenon, which is based on the energy transfer between light and matter, allows the identification of specific pigments by analyzing their emission spectra. The mechanism of fluorescence, illustrated in Fig. 6.1 a), involves the absorption of a photon with energy $E = h\nu$, where h is Planck's constant and ν is the frequency of the light. When a molecule absorbs a photon, it is excited from its ground state to a singlet excited state. Following excitation, the molecule undergoes relaxation through non-radiative transitions before eventually returning to the ground state, releasing energy in the form of light. The emitted light, called *fluorescence*, has a longer wavelength than the light used to excite the molecule.

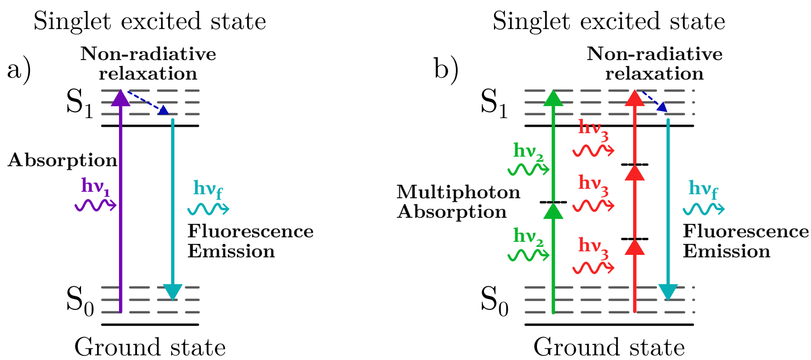

Figure 6.1: Jablonski diagrams of a) conventional fluorescence and b) multiphoton excited fluorescence (green: 2-photon excited fluorescence; red: 3-photon excited fluorescence).

In 1990, Winfried Denk *et al.* introduced a novel microscopy fluorescence technique based on a nonlinear process, where instead of using a single photon to excite a sample, two photons were used. This technique, known as two-photon fluorescence microscopy (2PFM) [100], differs from conventional fluorescence as it involves multiphoton absorption (MPA). In multiphoton excited fluorescence (MPEF), N photons with longer wavelengths are simultaneously absorbed to reach the same energy level as that of a single photon, as illustrated in Fig. 6.1 b).

Theoretically, this nonlinear process, in which N photons are simultaneously absorbed, is described by the high-order electric susceptibility χ^{2N-1} of the material, and by the N-photon cross-section $\sigma^{(N)}$, which determines the transition rate per atom $R^{(N)}$ [101]. The multiphoton transition rate is given by

$$R^{(N)} = \sigma^{(N)} I^N, \tag{6.1}$$

where I represents the intensity of the laser field. As shown in Eq. 6.1, MPA depends on the laser intensity; therefore, lasers with high peak power are required to induce this nonlinear phenomenon.

Experimentally, MPEF offers some advantages over conventional fluorescence. In multiphoton excitation microscopy, the laser source is focused to achieve MPA within the sample. In this setup, the laser beam is focused in a small region of the focal plane, where the intensity is high enough to induce multiphoton excitation. Outside this focal region, the photon flux is too low to generate any residual fluorescence signal, as shown in Fig. 6.2. This characteristic of the MPE process enables optical sectioning and improves spatial resolution. Moreover, the significant separation between excitation and emission wavelengths results in a high signal-to-noise ratio.

In Heritage Sciences, MPE has been applied in various investigations, as it allows both structural and compositional studies. The technique allows for the analysis of multilayered samples since MPE microscopy enables depth scans with high axial resolution [102, 103]. With this in mind, MPEF has been successfully applied to materials such as stained glass [103], wood [104], and pigments, including barium chromate, ochre yellow, titanium white [105], red lead, cadmium yellow, and Egyptian blue [102], among others. MPEF has also been proposed for use in archaeological research [106].

Since MPEF uses long wavelengths, it is considered a non-invasive technique. However, the requirement for high-power sources to induce MPE presents a significant challenge, as it can lead to photochemical damage to

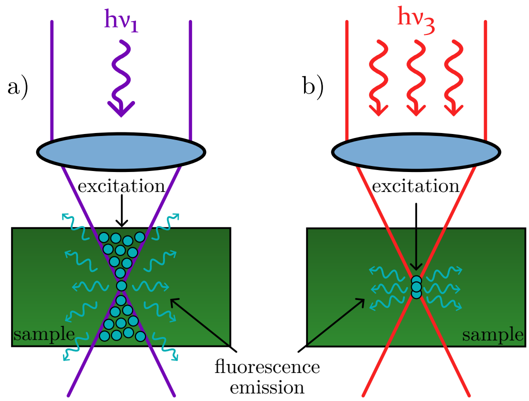

Figure 6.2: Schematic comparison between a) one-photon fluorescence and b) multiphoton fluorescence. Unlike linear fluorescence, in multiphoton fluorescence, the sample is excited in a small region where the laser beam is focused.

the samples [107]. This limitation is one of the most critical challenges in applying this multiphoton phenomenon to Heritage Sciences, but it also represents an opportunity to further explore and refine the technique.

6.1.1. MPEF investigation

To explore MPEF in our facilities, we focused on three commercially available Kremer pigments: cadmium sulfide (CdS), also known as cadmium yellow; zinc sulfide (ZnSO4); and titanium dioxide (TiO2), also known as titanium white. The pigments were prepared as tempera paint, using a binder made with 700 μl of egg yolk, 300 μl of distilled water, and 200 μl of linseed oil. The amount of pigment for each sample was chosen to give the paint a proper consistency. The tempera paint was applied to microscope slides, and an additional sample of binder was also prepared. The four samples are shown in Fig. 6.3.

To generate MPA, we used a Zeiss LSM-710-NLO confocal microscope. The laser source was a Chameleon Vision II titanium-sapphire tunable

Figure 6.3: Tempera samples analyzed using multiphoton excited fluorescence.

pulsed laser (140 fs) with a wavelength range of 680–1080 nm. The laser was focused using an EC EpiPlan 10X/0.2 objective in transmission geometry. The emission spectrum was recorded using a 32-channel photomultiplier tube, with a detection range from 431.3 nm to 727.4 nm and a resolution of approximately 9.7 nm. The excitation wavelength (λ_{exc}) was varied in 20 nm steps, from 760 nm to 940 nm. The laser power depended on the selected wavelength, with a maximum power at the sample of 3 mW at 800 nm. All measurements were performed using 3% of the laser power as indicated by the software, though the actual laser power incident on the sample was not specified. The results of our measurements are shown in Fig. 6.4.

The binder spectra, shown in Fig. 6.4 a), exhibit a maximum emission at 480 nm, with the amplitude decreasing as the excitation wavelength (λ_{exc}) decreases. The presence of random noise in the recorded signals indicates low fluorescence emission. The same emission spectrum was observed in the recorded signals for titanium dioxide and zinc sulfide, as shown in Fig. 6.4 c) and d), respectively. In all samples, the peak near 750 nm corresponds to $\lambda_{\mathrm{exc}} = 760$ nm, with variations in amplitude attributed to rescaling applied by the software during each sample measurement.

Our main observations were for cadmium sulfide and zinc sulfide, where we detected both fluorescence emission and second harmonic generation (SHG). For cadmium sulfide, we observed fluorescence emission peaks at approximately 509 nm and 793 nm, as shown in Fig. 6.4 b). The maximum

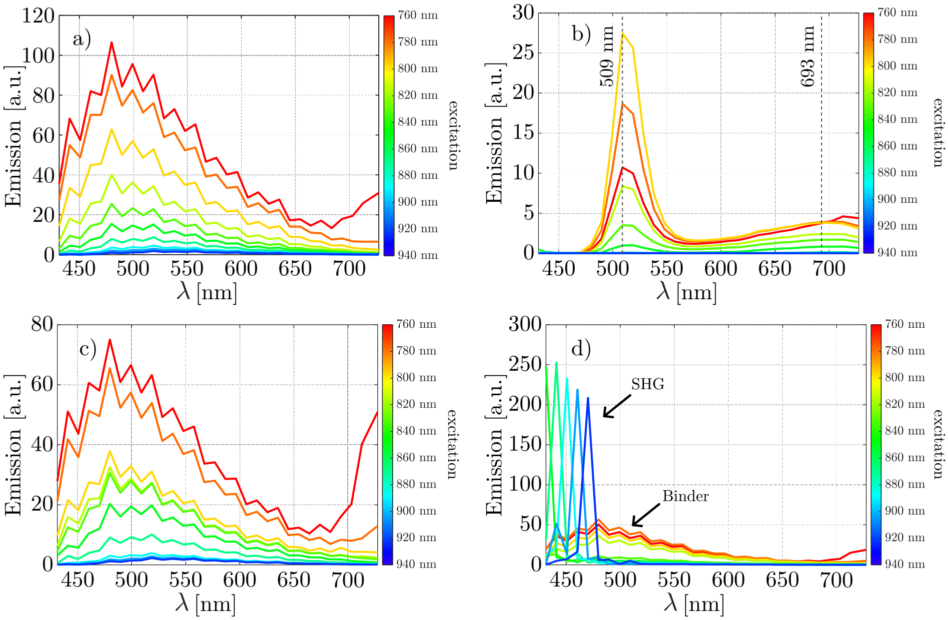

Figure 6.4: Emission spectra for a) binder, b) cadmium sulfide, c) titanium dioxide, and d) zinc sulfide.

amplitude emission was recorded with an excitation wavelength (λ_{exc}) of 800 nm. To study the photon absorption of cadmium sulfide, we measured the laser power reaching the sample using a power meter at $\lambda_{\mathrm{exc}} = 800$ nm. The subsequent analysis focused on the peak emission at 509 nm. The results are presented in Fig. 6.5 a).

Since the fluorescence intensity I_{fluo} is power-dependent on the incident laser intensity, following the relation $I_{\mathrm{fluo}} \propto I_{\mathrm{exc}}^{N}$ [108], where N is the number of photons simultaneously absorbed and I_{exc} is the laser intensity, we can take the natural logarithm of both the excitation and emission intensities and fit a linear function. The slope of this linear fit gives us the number of simultaneous photons absorbed in cadmium sulfide. The results, shown in Fig. 6.5 b), indicate a slope of 3.07 ± 0.01, corresponding to a

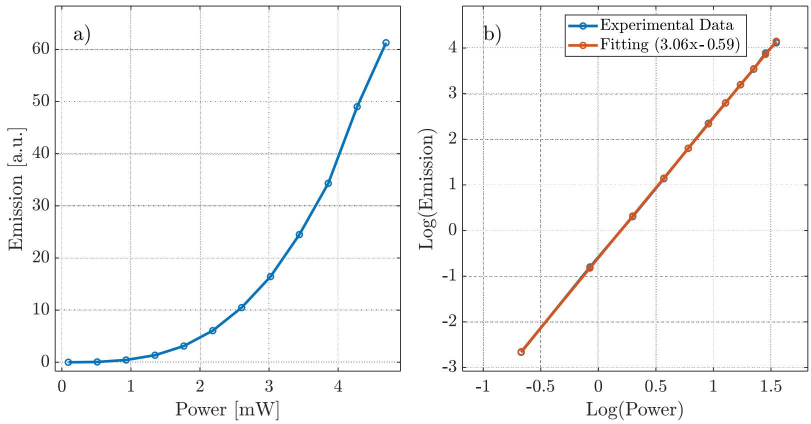

Figure 6.5: Three-photon absorption of cadmium sulfide. a) Fluorescence emission as a function of laser power. b) Linear fit of the natural logarithm of both emission and laser power, yielding a slope of 3.06, corresponding to three-photon absorption.

cubic dependence or three-photon absorption phenomenon. This behavior has been reported previously in cultural heritage investigations [102] and in CdS nanocrystals [109]. On the other hand, the emission band at 793 nm, which was not studied in this work, corresponds to trap states in the CdS particles. Trap states are defined as crystalline defects in semiconductors and do not depend on the cube of the incident intensity [110, 109].

Additionally, we observed evidence of second harmonic generation (SHG) in both cadmium sulfide and zinc sulfide. SHG is a nonlinear optical process in which a sample irradiated with a laser beam of frequency ω generates radiation at the second-harmonic frequency 2ω, as illustrated in the inset of Fig. 6.6 a). The second-order nonlinear susceptibility, $\chi^{(2)}$, of a medium determines its tendency to generate SHG. In the emission spectra of cadmium sulfide, shown in Fig. 6.4 b), SHG is not observed due to the strong emission at 509 nm. However, in another dataset, presented in Fig. 6.6 a), where excitation wavelengths λ_{exc} of 900, 950, 1000, and 1050 nm were used, we observed emission peaks at 450, 470, 500, and 528 nm, respectively.

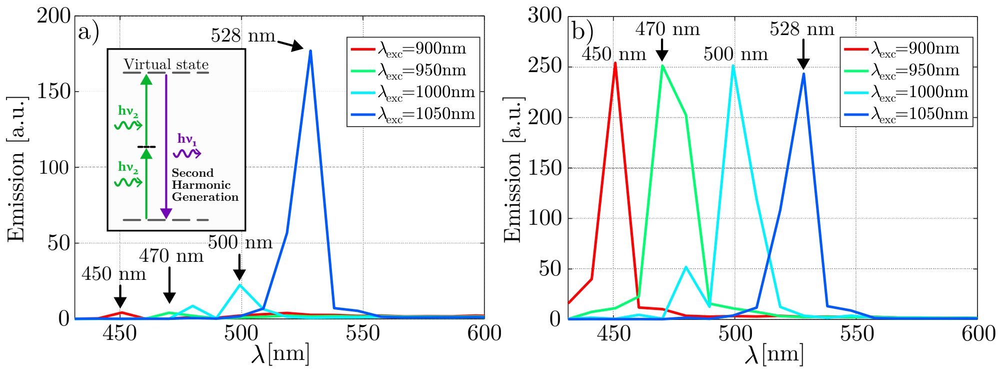

Figure 6.6: SHG in a) cadmium sulphide and b) zinc sulfide. The inset in a) illustrates the SHG mechanism

The reason we did not observe emission exactly at half of λ_{exc} is attributed to the resolution of the photodetection system. We recorded the maximum emission with $\lambda_{\text{exc}} = 1050$ nm. Although SHG has been reported in cadmium sulfide nanowires [111] and microcrystals [112] using the same range of λ_{exc} that we used, there is no documented evidence of SHG in commercial pigments or within the field of cultural heritage.

Regarding zinc sulfide, in addition to the spectra shown in Fig. 6.4 d), we also measured emission spectra with $\lambda_{\text{exc}} = 900$, 950, 1000 and 1050 nm. The results are presented in Fig. 6.6 b). Unlike cadmium sulfide, which exhibits maximum emission with $\lambda_{\text{exc}} = 1050$ nm, the optimal excitation wavelength for generating maximum emission in zinc sulfide is not clear. While SHG in zinc sulfide has been reported in optically polished polycrystalline samples [113], thin films [114], and nanowires [115], there is a lack of evidence for SHG in zinc sulfide pigments.

This result offers a new approach to analyzing pigments in uncontrolled environments, distinct from the above-mentioned investigations conducted on highly controlled nanostructures or thin films. In this study, we observed SHG and MPEF in commercially available pigments, which suggests the possibility of applying these non-linear optical techniques directly to real-world cultural heritage objects where pigments are often degraded, mixed, or applied in complex stratigraphies. Moreover, this discovery opens the door to using SHG as a non-invasive tool for pigment characterization in the field of cultural heritage, offering valuable insights into the material properties of historical artworks and artifacts. In addition, these results provide a basis for further exploration of how these optical phenomena manifest in commercial pigments under different environmental conditions and excitation wavelengths, potentially leading to new methodologies for pigment identification and conservation practices.

6.2. Future work

As mentioned at the beginning of this chapter, we have presented only the most relevant results; however, there are several potential avenues for future work.

In the case of cadmium sulfide, although we confirmed three-photon absorption and fluorescence emission, the emission peak center differs from other reported studies [116], where peaks were observed between 550 and 570 nm. It is likely that the particle size of the pigment in this study may have caused a shift in the emission peaks. Additionally, the emission corresponding to trap states is of interest as it provides morphological information about the pigment. The relevance of studying the interaction of light with this pigment using the mechanism exposed in this chapter lies in the fact that cadmium sulfide tends to lose color when exposed to light, making it subject of interest for studying degradation mechanisms [116, 117].

Regarding SHG in cadmium sulfide, this phenomenon has been minimally explored in cultural heritage science, offering an opportunity to investigate cadmium sulfide identification mechanisms further. It will be necessary to carefully study this nonlinear phenomenon to establish parameters for efficient SHG generation. Moreover, SHG could be applied to stratigraphic studies, as demonstrated in [102], where non-invasive techniques were used to analyze layered structures in artworks. By leveraging SHG in stratigraphic investigations, it may be possible to detect the presence of cadmium sulfide in complex, multilayered materials.

Finally, since both MPEF and SHG are nonlinear phenomena that require high power for generation, it is crucial to investigate potential photodamage caused by using such power levels. Given that one of the primary goals of these studies is to provide information that aids in the preservation and restoration of artistic and historical artifacts, it is essential to ensure that no damage is inflicted during the analysis. This requires a meticulous evaluation of the power thresholds that can be safely applied without compromising the integrity of the materials being studied.

Chapter 7

Conclusions

In this thesis, we have demonstrated the potential of non-destructive techniques, specifically THz-TDS and MPEF, for investigating culturral heritage objects, with a particular focus on stratigraphy analysis and pigment characterization. Through the development and implementation of signal processing algorithms, alongside the application of nonlinear optics as a potential tool in cultural heritage field, this research has shown the capability of these methods to reveal hidden layers and identify material compositions, aiming to minimize direct intervention in heritage artifacts.

The relevance of signal processing in THz signals was showed in Chapter 3, where an algoritm for calculation the cutoff frequency was presented. We found that by smoothing and multiplying THz spectra by a cubic function, it is possible to determine the frequency at which the usable bandwidth decays to the noise floor. This method can be applied to any signal from any THz-TDS system, since this method analyzes the spectrum itself and does not depend on either the system configuration or the optical parameters of the sample. Moreover, the algorithm proves practical for analyzing large volumes of spectra, such as those found in a THz image.

The analysis of the wooden gilded tablet *Our Lady of Kazan*, presented in Chapter 4, exemplifies the utility of THz-TDI for pigment mapping, particularly for pigments exhibiting spectral features in the THz range. In this study, involving approximately 250,000 THz traces, we implemented the algorithm for Chapter 3 to calculate the cutoff frequency. This allowed us to generate a mercury sulfide (HgS) map, which presents a spectral footprint at 1.14 THz, by analyzing spectra with a cutoff frequency beyond 1.45 THz. This method enhanced the precision of non-invasive pigment identification through THz imaging, as presented in my master's thesis, by eliminating 84% of the noisy spectra that were originally considered as positive to HgS. It is important to highlight that this technique is completely safe for both the artwork and the operator, in contrast to other pigment mapping methods such as Macro-XRF imaging, which uses ionizing radiation.

Furthermore, THz-TDI proved highly effective for studying multilayer systems via cross-sectional imaging. By employing algorithms such as sparse deconvolution, presented also in Chapter 4, we were able to identify overlapping echoes, allowing for accurate stratigraphic analysis as an alternative to traditional deconvolution techniques and spectral filtering. When applied to the Russian Icon THz image, the algorithm revealed at least seven layers, including one visible only in specific areas of the faces of the characters. Additionally, this approach helped distinguish the original canvas from the new canvas in Pablo Picasso's painting *Homme au chapeau*, enhancing contrast in the raw THz images previously presented by Dr. Fukunaga. This further highlights the technique's applicability in examining complex structures within cultural heritage objects, providing a non-invasive method for stratigraphy composition analysis.

In Chapter 5, we presented 3D SAR THz-TDS imaging, with a focus on multilayered samples and complex-shaped objects. We demonstrated the capability of this technique to identify hidden layers and painted figures while also reconstructing intricate shapes of these objects. This study highlights how 3D SAR THz-TDS overcomes previous limitations in scanning cultural heritage objects with irregular geometries, expanding the range of items that can be analyzed using THz techniques without requiring additional engineering, such as robotic arms previously reported in the literature.

Regarding pigment identification through nonlinear optics, as presented in the final Chapter, we confirmed the use of MPEF to identify cadmium sulfide via a three-photon absorption mechanism. Additionally, we provided preliminary results indicating SHG in both cadmium sulfide and zinc sulfide in commercial pigments, a phenomenon that has not been previously reported in the field. These findings open new insights into the nonlinear optical properties of these materials and expanding the analytical techniques available for pigment characterization

While this thesis presents significant results, there are limitations and challenges that remain. Although sparse deconvolution assists in identifying overlapping echoes, it does not account for the dispersion of the reflected echoes, which, in some cases, can lead to misinterpretations. Additionally, there is no established protocol for defining the regularization parameter λ, a critical factor in the iteration process for interface identification in raw data.

Similarly, while 3D THz-TDS SAR imaging represents a promising alternative to THz-TDI for analyzing objects with irregular shapes, the low SNR caused by the absence of focusing lenses can lead to inaccuracies in stratigraphic analysis, as demonstrated with Sample two in Chapter 5. Denoising algorithms and edge detection methods applied to traces and radargrams could address this issue on the resulting images. An important factor to consider is the total data acquisition time required for radargram recording. In the cases presented here, the acquisition time ranged between 24 and 48 hours, which could be impractical for in situ measurements. Additionally, it is essential to have adequate computer resources to minimize data processing time.

In the case of nonlinear optics applied to pigment studies, it is crucial to further investigate the potential photochemical damage caused by the high-power laser sources used in these techniques. Understanding the threshold at which laser exposure begins to alter the chemical structure of pigments or cause degradation is essential for ensuring that these methods remain non-invasive. Additionally, the cumulative effects of repeated measurements on fragile or sensitive materials should be explored.

In conclusion, this thesis has demonstrated the efficacy of advanced optical techniques in preventive conservation and art preservation research. By providing new insights into non-invasive diagnostic tools, it contributes to the broader goal of preserving cultural heritage for future generations. These findings serve as a foundation for continued exploration of how optical methods can be integrated into conservation practices, ultimately improving the sustainability of cultural heritage management.

Bibliography

[1] UNESCO. *2009 UNESCO framework for cultural statistics.* UNESCO Institute for Statistics, 2009.

[2] Internation Counsil of Museum - Committee for Conservation. Terminology to characterize the conservation of tangible cultural heritage. In *Resolution Adopted by the ICOM-CC Membership at the 15th Triennial Conference*, New Delhi, September 22-26 2008.

[3] Michael D. Glascock. Archaeometry. In Deborah M. Pearsall, editor, *Encyclopedia of Archaeology*, pages 489–494. Academic Press, New York, 2008.

[4] Luís Manuel de Almeida Nieto, Francesca Gabrieli, Annelies van Loon, Victor Gonzalez, Joris Dik, Raf Van de Plas, and Matthias Alfeld. Comparison of macro x-ray fluorescence and reflectance imaging spectroscopy for the semi-quantitative analysis of pigments in easel paintings: A study on lead white and blue verditer. *X-Ray Spectrometry*, n/a(n/a), 2023.

[5] Marco Colombo, Falk Münch, Peter Hoffmann, Jochen Sander, and Wolfgang Ensinger. Scanning macro x-ray fluorescence spectroscopy maps for matching 17th century paintings color areas to different earth pigments uses and for investigating attribution issues. *X-Ray Spectrometry*, 53(2):139–152, 2023.

[6] Matthias Alfeld and Koen Janssens. Strategies for processing megapixel X-ray fluorescence hyperspectral data: a case study on a version of Caravaggio's painting Supper at Emmaus. *Journal of Analytical Atomic Spectrometry*, 30:777–789, 2015.

[7] Tiziana Cavaleri, Claudia Pelosi, Marco Ricci, Stefano Laureti, Francesco Paolo Romano, Claudia Caliri, Bernadette Ventura, Stefania De Blasi, and Marco Gargano. IR Reflectography, Pulse-Compression Thermography, MA-XRF, and Radiography: A Full-Thickness Study of a 16th-Century Panel Painting Copy of Raphael. *Journal of Imaging*, 8(6), 2022.

[8] Claudia Caliri, Marina Bicchieri, Paola Biocca, and Francesco Paolo Romano. In situ macro X-Ray fluorescence scanning on a Leonardo da Vinci portrait. *X-Ray Spectrometry*, 50(4):332–340, 2021.

[9] Theofanis Gerodimos, Anastasios Asvestas, Georgios P. Mastrotheodoros, Giannis Chantas, Ioannis Liougos, Aristidis Likas, and Dimitrios F. Anagnostopoulos. Scanning X-ray Fluorescence Data Analysis for the Identification of Byzantine Icons' Materials, Techniques, and State of Preservation: A Case Study. *Journal of Imaging*, 8(5), 2022.

[10] Małgorzata Walczak, Dominika Tarsińska-Petruk, Michał Płotek, Maria Goryl, and Mirosław P. Kruk. MA-XRF study of 15th–17th century icons from the collection of the National Museum in Krakow, Poland. *X-Ray Spectrometry*, 48(4):303–310, 2019.

[11] Maurizio Aceto, Angelo Agostino, Gaia Fenoglio, Ambra Idone, Monica Gulmini, Marcello Picollo, Paola Ricciardi, and John K. Delaney. Characterisation of colourants on illuminated manuscripts by portable fibre optic UV-visible-NIR reflectance spectrophotometry. *Analytical Methods*, 6:1488–1500, 2014.

[12] F. Salvemini, E. Barzagli, F. Grazzi, M. Picollo, A. Agostino, M.G. Roselli, and M. Zoppi. An in situ non-invasive study of two Tibetan manuscripts from the Asian Collection of the Museum of Natural History in Florence. *Archaeological and Anthropological Sciences*, 10(8):1881 – 1901, 2018.

[13] Maurizio Aceto, Angelo Agostino, Gaia Fenoglio, Ambra Idone, Fabrizio Crivello, Martina Griesser, Franz Kirchweger, Katharina Uhlir, and Patricia Roger Puyo. Analytical investigations on the Coronation Gospels manuscript. *Spectrochimica Acta Part A: Molecular and Biomolecular Spectroscopy*, 171:213–221, 2017.

[14] Abdelmajid El Bakkali, Taibi Lamhasni, Saadia Ait Lyazidi, Mustapha Haddad, Francesca Rosi, Costanza Miliani, Santiago Sánchez-Cortés, and Mustapha El Rhaiti. Assessment of a multi-technical non-invasive approach for the typology of inks, dyes and pigments in two 19th century's ancient manuscripts of Morocco. *Vibrational Spectroscopy*, 74:47–56, 2014.

[15] Sara Barbache, Taibi Lamhasni, Abdelmajid El Bakkali, Saadia Ait Lyazidi, Mustapha Haddad, Abdelouahed Ben-Ncer, and Mohamed Hnach. Optical analyses of wool dyeing materials in ancient Moroccan carpets "Zarbia(s)": Combination of UV-vis diffuse reflectance, 3D-fluorescence and Raman spectroscopies. *Dyes and Pigments*, 153:256 – 265, 2018.

[16] C. Clementi, C. Miliani, A. Romani, U. Santamaria, F. Morresi, K. Mlynarska, and G. Favaro. In-situ fluorimetry: A powerful non-invasive diagnostic technique for natural dyes used in artefacts: Part II. Identification of orcein and indigo in Renaissance tapestries. *Spectrochimica Acta Part A: Molecular and Biomolecular Spectroscopy*, 71(5):2057–2062, 2009.

[17] A. Galli, G. Poldi, M. Martini, E. Sibilia, C. Montanari, and L. Panzeri. Study of blue colour in ancient mosaic tesserae by means of thermoluminescence and reflectance measurements. *Applied Physics A*, 83(4):675–679, 2006.

[18] Wang Bin, Yu Hui, Guy Bovyn, and Joost M. A. Caen. In situ investigation of Chinese export watercolours in the nineteenth century: Pigments and dyes. *Journal of the Institute of Conservation*, 41(3):218 – 234, 2018.

[19] Vittoria Guglielmi, Chiara Andrea Lombardi, Giacomo Fiocco, Valeria Comite, Andrea Bergomi, Mattia Borelli, Monica Azzarone, Marco Malagodi, Mario Colella, and Paola Fermo. Multi-Analytical Investigation on a Renaissance Polychrome Earthenware Attributed to Giovanni Antonio Amadeo. *Applied Sciences (Switzerland)*, 13(6), 2023.

[20] Alireza Koochakzaei, Elmira Mobasher Maghsoud, and Behrooz Jelodarian Bidgoli. Non-invasive imaging and spectroscopy techniques for identifying historical pigments: a case study of Iranian manuscripts from the Qajar era. *Heritage Science*, 11(1), 2023.

[21] Na Ra Lee, Ji Hyeon Yun, and So Jin Kim. Raman spectroscopy of yellow organic pigments of large Korean Buddhist paintings from the late Joseon dynasty (17th–19th centuries). *Journal of Raman Spectroscopy*, 54(8):836 – 846, 2023.

[22] Eugenia Tomasini, Ilaria Costantini, Valeria Careaga, Carlos Rua Landa, Kepa Castro, Juan Manuel Madariaga, Marta Maier, and Gabriela Siracusano. Identification of pigments and binders of a 17th century mural painting (Bolivia). New report on pigments associated with Andean minerals. *Journal of Cultural Heritage*, 62:206 – 216, 2023.

[23] Letizia Bonizzoni, Simone Caglio, Anna Galli, Chiara Germinario, Francesco Izzo, and Donata Magrini. Identifying Original and Restoration Materials through Spectroscopic Analyses on Saturnino Gatti Mural Paintings: How Far a Noninvasive Approach Can Go. *Applied Sciences (Switzerland)*, 13(11), 2023.

[24] A. Sarmiento, M. Pérez-Alonso, M. Olivares, K. Castro, I. Martínez-Arkarazo, L.A. Fernández, and J.M. Madariaga. Classification and identification of organic binding media in artworks by means of Fourier transform infrared spectroscopy and principal component analysis. *Analytical and Bioanalytical Chemistry*, 399(10):3601 – 3611, 2011.

[25] María Teresa Molina, Emilio Cano, Joaquina Leal, Rafael Fort, Mónica Álvarez de Buergo, and Blanca Ramírez-Barat. Protective Coatings for Metals in Scientific—Technical Heritage: The Collection of the Spanish National Museum of Science and Technology (MUNCYT). *Heritage*, 6(3), 2023.

[26] Elizabeth Dickinson and Kirsty E. High. The use of infrared spectroscopy and chemometrics to investigate deterioration in vegetable tanned leather: potential applications in heritage science. *Heritage Science*, 10(1), 2022.

[27] Giorgia Sciutto, Paolo Oliveri, Silvia Prati, Emilio Catelli, Irene Bonacini, and Rocco Mazzeo. A Multivariate Methodological Workflow for the Analysis of FTIR Chemical Mapping Applied on Historic Paint Stratigraphies. *International Journal of Analytical Chemistry*, 2017, 2017.

[28] M.L. Franquelo, A. Duran, L.K. Herrera, M.C. Jimenez de Haro, and J.L. Perez-Rodriguez. Comparison between micro-Raman and

micro-FTIR spectroscopy techniques for the characterization of pigments from Southern Spain Cultural Heritage. *Journal of Molecular Structure*, 924-926(C):404 – 412, 2009.

[29] M. Oujja, F. Agua, M. Sanz, D. Morales-Martin, M. García-Heras, M.A. Villegas, and M. Castillejo. Multiphoton Excitation Fluorescence Microscopy and Spectroscopic Multianalytical Approach for Characterization of Historical Glass Grisailles. *Talanta*, 230:122314, 2021.

[30] Alice Dal Fovo, Mikel Sanz, Mohamed Oujja, Raffaella Fontana, Sara Mattana, Riccardo Cicchi, Piotr Targowski, Marcin Sylwestrzak, Aldo Romani, Chiara Grazia, George Filippidis, Sotiris Psilodimitrakopoulos, Andreas Lemonis, and Marta Castillejo. In-Depth Analysis of Egg-Tempera Paint Layers by Multiphoton Excitation Fluorescence Microscopy. *Sustainability*, 12(9), 2020.

[31] A. Dal Fovo, M. Sanz, S. Mattana, M. Oujja, M. Marchetti, F.S. Pavone, R. Cicchi, R. Fontana, and M. Castillejo. Safe limits for the application of nonlinear optical microscopies to cultural heritage: A new method for in-situ assessment. *Microchemical Journal*, 154:104568, 2020.

[32] P.R. Smith, D.H. Auston, and M.C. Nuss. Subpicosecond photoconducting dipole antennas. *IEEE Journal of Quantum Electronics*, 24(2):255–260, 1988.

[33] Lulu Wang. Terahertz Imaging for Breast Cancer Detection. *Sensors*, 21(19), 2021.

[34] Goretti G. Hernandez-Cardoso, Lauro F. Amador-Medina, Gerardo Gutierrez-Torres, Edgar S. Reyes-Reyes, César Augusto Benavides Martínez, Cuitlahuac Cardona Espinoza, José Arce Cruz, Irv-

ing Salas-Gutierrez, Blanca O. Murillo-Ortíz, and Enrique Castro-Camus. Terahertz imaging demonstrates its diagnostic potential and reveals a relationship between cutaneous dehydration and neuropathy for diabetic foot syndrome patients. *Scientific Reports*, 12(1):3110, 2022.

[35] Yu Zhang, Juan Han, Dan Wang, Xiao Li, Tianzhu Qiu, Hua Chen, and Xiaofeng Chen. Application of THz Time-Domain Spectroscopy to Diagnose Gastric Cancer Tissues in Surgical Resected Specimens. *Journal of Infrared, Millimeter, and Terahertz Waves*, 42(7):802 – 812, 2021.

[36] Zhang Zhenwei, Xu Jing, Jia Rui, Wu Yinghong, Guan Hao, Han Siyi, Zhang Cunlin, and Zhao Yuejin. Terahertz Non-Destructive Testing and Imaging of High-Voltage Cables. *Frontiers in Physics*, 10, 2022.

[37] Qiang Wang, Xinyi Li, Tianying Chang, Jin Zhang, Lingyu Liu, Hongbin Zhou, and Jinpeng Bai. Nondestructive imaging of hidden defects in aircraft sandwich composites using terahertz time-domain spectroscopy. *Infrared Physics & Technology*, 97:326–340, 2019.

[38] Leili Afsah-Hejri, Elnaz Akbari, Arash Toudeshki, Taymaz Homayouni, Azar Alizadeh, and Reza Ehsani. Terahertz spectroscopy and imaging: A review on agricultural applications. *Computers and Electronics in Agriculture*, 177:105628, 2020.

[39] Wei Liu, Changhong Liu, Xiaohua Hu, Jianbo Yang, and Lei Zheng. Application of terahertz spectroscopy imaging for discrimination of transgenic rice seeds with chemometrics. *Food Chemistry*, 210:415–421, 2016.

[40] Andreja Abina, Uroš Puc, Anton Jeglič, and Aleksander Zidanšek. Applications of Terahertz Spectroscopy in the Field of Construction and Building Materials. *Applied Spectroscopy Reviews*, 50(4):279–303, 2015.

[41] Jyotirmayee Dash, Shaumik Ray, Kathirvel Nallappan, Saptarshi Sasmal, and Bala Pesala. Non-destructive inspection of internal defects in concrete using continuous wave 2D terahertz imaging system. In *2013 38th International Conference on Infrared, Millimeter, and Terahertz Waves (IRMMW-THz)*, pages 1–2, 2013.

[42] Xuelei Jiang, Ying Xu, Hang Hu, and Wenyu Xie. Nondestructive testing of corrosion thickness in coated steel structures with THz-TDS. *Measurement: Journal of the International Measurement Confederation*, 217:113088, 2023.

[43] Moritz Anuschek, Anne Linnet Skelbæk-Pedersen, Thomas Kvistgaard Vilhelmsen, Erik Skibsted, J. Axel Zeitler, and Jukka Rantanen. Terahertz time-domain spectroscopy for the investigation of tablets prepared from roller compacted granules. *International Journal of Pharmaceutics*, 642:123165, 2023.

[44] Moritz Anuschek, Thomas Kvistgaard Vilhelmsen, J. Axel Zeitler, and Jukka Rantanen. Towards simultaneous determination of tablet porosity and height by terahertz time-domain reflection spectroscopy. *International Journal of Pharmaceutics*, 646:123424, 2023.

[45] Taeyoon Hong, Kyujin Choi, Taewoo Ha, Byung Cheol Park, Kyung Ik Sim, Jong Hyeon Kim, Jae Hoon Kim, Jy Eun Kwon, Sanghyun Lee, Dai Ill Kang, and Han Hyoung Lee. Terahertz time-domain and Fourier-transform infrared spectroscopy of traditional Korean pigments. *Journal of the Korean Physical Society*, 64(5):727 – 731, 2014.

[46] Alessia Artesani, Raffaella Lamuraglia, Federica Menegazzo, Stefano Bonetti, and Arianna Traviglia. Terahertz Time-Domain Spectroscopy in Reflection Configuration for Inorganic and Mineral Pigment Identification. *Applied Spectroscopy*, 77(1):74 – 87, 2023.

[47] Candida Moffa, Camilla Merola, Fernando Piamonte Magboo, Enrica Chiadroni, Lucia Giuliani, Alessandro Curcio, Luigi Palumbo, Anna Candida Felici, and Massimo Petrarca. Pigments, minerals, and copper-corrosion products: Terahertz continuous wave (THz-CW) spectroscopic characterization of antlerite and atacamite. *Journal of Cultural Heritage*, 66:483 – 490, 2024.

[48] Rosarosa Manca, Laura Chiarantini, Edoardo Tartaglia, Francesco Soldovieri, Costanza Miliani, and Ilaria Catapano. Non-Invasive Characterization of Maiolica Layer Structure by Terahertz Time-Domain Imaging. *Coatings*, 13(7), 2023.

[49] Kaori Fukunaga, Yoshimi Ueno, Chihiro Watanabe, Akinobu Yanagida, and Soichiro Wakiya. Nondestructive Observation of Multilayered Paintings on a Single Canvas by THz Time-Domain Imaging and X-ray Fluorescence Elemental Mapping. *Journal of Infrared, Millimeter, and Terahertz Waves*, 45(1-2):124 – 140, 2024.

[50] Corinna L. Koch Dandolo, Gilda María Pasco Saldaña, Mirta Asunción Insaurralde Caballero, Monserrat Alma Gómez Sepúlveda, Arturo Ignacio Hernández-Serrano, Alejandro Mesa Orozco, Joselyn Alvarado Calderón, Melba Samara Calderón Zárate, Karen Luna González, Eunice Corazón Peralta de Dios, Gerardo Hernández Rosales, and Enrique Castro-Camus. Terahertz Time-Domain Imaging to Guide a Conservation Intervention on a Stratified Easel Painting. *Journal of Infrared, Millimeter, and Terahertz Waves*, 39(8):773 – 784, 2018.

[51] Vivi Tornari, Michalis Andrianakis, Stéphanie Duchêne, Witold Nowik, Didier Brissaud, David Giovannacci, Markus Küppers, Christian Rehorn, Bernhard Blümich, Giulia Ricci, and Gilberto Artioli. A combined ND diagnostic investigation by DHSPI, SIRT, NMR, THZ, on Giotto fresco. *Journal of Cultural Heritage*, 63:206 – 216, 2023.

[52] Alessia Artesani, Francesco Abate, Raffaella Lamuraglia, Maria Antonietta Baldo, Federica Menegazzo, and Arianna Traviglia. Integrated Imaging and Spectroscopic Analysis of Painted Fresco Surfaces Using Terahertz Time-Domain Technique. *Heritage*, 6(7):5202 – 5212, 2023. All Open Access, Gold Open Access.

[53] Corinna L. Koch Dandolo, Antonino Cosentino, and Peter Uhd Jepsen. Inspection of panel paintings beneath gilded finishes using terahertz time-domain imaging. *Studies in Conservation*, 60:S159 – S166, 2015.

[54] Frances E. M. Lambert, Jan Ornik, Naja-Anissa Staats, Alexander Jäckel, Goretti G. Hernandez-Cardoso, Jochen Taiber, Eva-Maria Stübling, Benjamin Rudolph, Oliver Mack, Hans Portsteffen, Enrique Castro-Camus, and Martin Koch. Layer separation mapping and consolidation evaluation of a fifteenth century panel painting using terahertz time-domain imaging. *Scientific Reports*, 12(1), 2022.

[55] K. Krügener, M. Schwerdtfeger, S.F. Busch, A. Soltani, E. Castro-Camus, M. Koch, and W. Viöl. Terahertz meets sculptural and architectural art: Evaluation and conservation of stone objects with T-ray technology. *Scientific Reports*, 5, 2015.

[56] F.E.M. Lambert, E.S. Reyes-Reyes, G.G. Hernandez-Cardoso, A.M. Gomez-Sepulveda, and E. Castro-Camus. In situ Determination of the State of Conservation of Paint Coatings on the Kiosk of Guadala-

jara Using Terahertz Time-Domain Spectroscopy. *Journal of Infrared, Millimeter, and Terahertz Waves*, 41(4):355 – 364, 2020.

[57] Kaori Fukunaga, Tomofumi Ikari, and Kikuko Iwai. THz pulsed time-domain imaging of an oil canvas painting: a case study of a painting by Pablo Picasso. *Applied Physics A: Materials Science and Processing*, 122(2):1 – 5, 2016.

[58] Ch. Fattinger and D. Grischkowsky. Point source terahertz optics. *Applied Physics Letters*, 53(16):1480–1482, 10 1988.

[59] P.R. Smith, D.H. Auston, and M.C. Nuss. Subpicosecond photoconducting dipole antennas. *IEEE Journal of Quantum Electronics*, 24(2):255–260, 1988.

[60] Ying Han, Yubin Guo, Bo Gao, Chunyang Ma, Ruohan Zhang, and Han Zhang. Generation, optimization, and application of ultrashort femtosecond pulse in mode-locked fiber lasers. *Progress in Quantum Electronics*, 71:100264, 2020.

[61] Yun-Shik Lee. *Principles of Terahertz Science and Technology*. Springer Publishing Company, Incorporated, 1st edition, 2008.

[62] A.M. Buryakov, M.S. Ivanov, S.A. Nomoev, D.I. Khusyainov, E.D. Mishina, V.A. Khomchenko, I.S. Vasil'evskii, A.N. Vinichenko, K.I. Kozlovskii, A.A. Chistyakov, and J.A. Paixão. An advanced approach to control the electro-optical properties of LT-GaAs-based terahertz photoconductive antenna. *Materials Research Bulletin*, 122, 2020.

[63] Nikita Vashistha, Mahesh Kumar, Rajiv K. Singh, Debiprasad Panda, Lavi Tyagi, and Subhananda Chakrabarti. A comprehensive study of ultrafast carrier dynamics of LT-GaAs: Above and below bandgap regions. *Physica B: Condensed Matter*, 602:412441, 2021.

[64] Mira Naftaly and Richard Dudley. Methodologies for determining the dynamic ranges and signal-to-noise ratios of terahertz time-domain spectrometers. *Opt. Lett.*, 34(8):1213–1215, Apr 2009.

[65] Edgar Santiago Reyes Reyes. Desarrollo de algoritmos para procesamientos de señales de THz para el análisis de objetos de valor cultural. Master's thesis, Centro de Investigaciones en Óptica, A.C., 2020.

[66] G.P. Mastrotheodoros, K.G. Beltsios, Y. Bassiakos, and V. Papadopoulou. On the Metal-Leaf Decorations of Post-Byzantine Greek Icons. *Archaeometry*, 60(2):269 – 289, 2018.

[67] Anne van Grevenstein, Britta New, Christina Young, Kate Seymour, Roger Groves, and Velson Horie. *The conservation of panel paintings and related objects: Research agenda 2014 -2020.* NWO, Netherlands Organisation for Scientific Research, The Hague, 2014.

[68] Emanuele D'Angelo. Development of computational three-dimensional THz-time domain hyperspectral imaging. Master's thesis, Department of Photonic Engineering, Technical University of Denmark, 2017.

[69] Renate Nöller. Cinnabar reviewed: characterization of the red pigment and its reactions. *Studies in Conservation*, 60(2):79–87, 2015.

[70] D. Chiriu, M. Pala, F.A. Pisu, G. Cappellini, P.C. Ricci, and C.M. Carbonaro. Time through colors: A kinetic model of red vermilion darkening from Raman spectra. *Dyes and Pigments*, 184:108866, 2021.

[71] Kerstin Elert, Manuel Pérez Mendoza, and Carolina Cardell. Direct evidence for metallic mercury causing photo-induced darkening of red cinnabar tempera paints. *Communications Chemistry*, 4(1), 2021.

[72] Elyse M. Kleist and Timothy M. Korter. Quantitative Analysis of Minium and Vermilion Mixtures Using Low-Frequency Vibrational Spectroscopy. *Analytical Chemistry*, 92(1):1211 – 1218, 2020.

[73] Junliang Dong, J. Bianca Jackson, Marcello Melis, David Giovanacci, Gillian C. Walker, Alexandre Locquet, John W. Bowen, and D.S. Citrin. Terahertz frequency-wavelet domain deconvolution for stratigraphic and subsurface investigation of art painting. *Optics Express*, 24(23):26972 – 26985, 2016.

[74] Junliang Dong, Xiaolong Wu, Alexandre Locquet, and David S. Citrin. Terahertz Superresolution Stratigraphic Characterization of Multilayered Structures Using Sparse Deconvolution. *IEEE Transactions on Terahertz Science and Technology*, 7(3):260 – 267, 2017.

[75] Bo Wang, Xiaoling Qin, Wenping Li, Zeren Li, and Liguo Zhu. Learned iterative shrinkage and thresholding algorithm for terahertz sparse deconvolution. *Optics Express*, 30(11):18238 – 18249, 2022.

[76] E.S. Reyes-Reyes, R. Carriles-Jaimes, and E. Castro-Camus. Algorithm for Determination of Cutoff Frequency of Noise Floor Level for Terahertz Time-Domain Signals. *Journal of Infrared, Millimeter, and Terahertz Waves*, 43(11-12):847 – 856, 2022.

[77] Edgar Santiago Reyes-Reyes, Ramón Carriles-Jaimes, Emanuele D'Angelo, Saad Nazir, Corinna Ludovica Koch-Dandolo, Falko Kuester, Peter Uhd Jepsen, and Enrique Castro-Camus. Terahertz time-domain imaging for the examination of gilded wooden artifacts. *Scientific Reports*, 14(1), 2024.

[78] K. Tomiyasu. Tutorial review of synthetic-aperture radar (SAR) with applications to imaging of the ocean surface. *Proceedings of the IEEE*, 66(5):563–583, 1978.

[79] Sean T. Peters, Dustin M. Schroeder, Mark S. Haynes, Davide Castelletti, and Andrew Romero-Wolf. Passive Synthetic Aperture Radar Imaging Using Radio-Astronomical Sources. *IEEE Transactions on Geoscience and Remote Sensing*, 59(11):9144 – 9159, 2021.

[80] Steven R. Wilkinson, Charlie Hansen, Barry Alexia, Bishara Shamee, Brian Lloyd, Anthony Beasley, Walter Brisken, Flora Paganelli, Galen Watts, Karen O'Neil, and Patrick Courtney. A Planetary Radar System for Detection and High-Resolution Imaging of Nearby Celestial Bodies. *Microwave Journal*, 65(1):22 – 42, 2022.

[81] Yu-Hang Zhou, Meng-Yu Hao, Wei-Zeng Shao, Armando Marino, Xin-Gai Song, and Xing-Wei Jiang. Preliminary analysis of wind and wave retrieval from Chinese 1mC-SAR image. *European Journal of Remote Sensing*, 57(1), 2024.

[82] Bolin Fu, Hongyuan Kuang, Yan Wu, Tengfang Deng, Weiwei Sun, Xiangjin Shen, Ertao Gao, Hongchang He, and Linhang Jiang. Mangrove species classification using novel adaptive ensemble learning with multi-spatial-resolution multispectral and full-polarization SAR images. *International Journal of Digital Earth*, 17(1), 2024.

[83] Muhammad Farhan Humayun, Faryal Aurooj Nasir, Farrukh Aziz Bhatti, Madiha Tahir, and Khurram Khurshid. YOLO-OSD: Optimized Ship Detection and Localization in Multiresolution SAR Satellite Images Using a Hybrid Data-Model Centric Approach. *IEEE Journal of Selected Topics in Applied Earth Observations and Remote Sensing*, 17:5345 – 5363, 2024.

[84] Zhichao Sun, Hang Ren, Huarui Sun, Gary G. Yen, Junjie Wu, and Jianyu Yang. Terminal Trajectory Planning for Synthetic Aperture Radar Imaging Guidance Based on Chronological Iterative Search

Framework. *IEEE Transactions on Cybernetics*, 54(5):3065 – 3078, 2024.

[85] Helena Cruz, Mário Véstias, José Monteiro, Horácio Neto, and Rui Policarpo Duarte. A Review of Synthetic-Aperture Radar Image Formation Algorithms and Implementations: A Computational Perspective. *Remote Sensing*, 14(5), 2022.

[86] Yinwei Li, Jiawei Wu, Qianqian Mao, Han Xiao, Fei Meng, Wenquan Gao, and Yiming Zhu. A Novel 2-D Autofocusing Algorithm for Real Airborne Stripmap Terahertz Synthetic Aperture Radar Imaging. *IEEE Geoscience and Remote Sensing Letters*, 20, 2023.

[87] Mavis Gezimati and Ghanshyam Singh. Curved Synthetic Aperture Radar for Near-Field Terahertz Imaging. *IEEE Photonics Journal*, 15(3), 2023. Cited by: 4.

[88] Li Yi, Ryohei Kaname, Ryoko Mizuno, Yihan Li, Masayuki Fujita, Hiroshi Ito, and Tadao Nagatsuma. Ultra-Wideband Frequency Modulated Continuous Wave Photonic Radar System for Three-Dimensional Terahertz Synthetic Aperture Radar Imaging. *Journal of Lightwave Technology*, 40(20):6719 – 6728, 2022.

[89] Dilyan Damyanov, Benedikt Friederich, Milad Yahyapour, Nico Vieweg, Anselm Deninger, Kevin Kolpatzeck, Xuan Liu, Andreas Czylwik, Thorsten Schultze, Ingolf Willms, and Jan C. Balzer. High Resolution Lensless Terahertz Imaging and Ranging. *IEEE Access*, 7:147704–147712, 2019.

[90] Dilyan Damyanov, Tobias Kubiczek, Kevin Kolpatzeck, Andreas Czylwik, Thorsten Schultze, and Jan C. Balzer. 3D THz-TDS SAR Imaging by an Inverse Synthetic Cylindrical Aperture. *IEEE Access*, 11:9680–9690, 2023.

[91] Tobias Kubiczek, Efe Satiroglu, Thorsten Schultze, and Jan C. Balzer. THz 3D Imaging Based on an Inverse Spherical Synthetic Aperture. In *2023 48th International Conference on Infrared, Millimeter, and Terahertz Waves (IRMMW-THz)*, pages 1–2, 2023.

[92] Gillian C. Walker, John W. Bowen, Julien Labaune, J-Bianca Jackson, Sillas Hadjiloucas, John Roberts, Gerard Mourou, and Michel Menu. Terahertz deconvolution. *Optics Express*, 20(25):27230–27241, Dec 2012.

[93] Junliang Dong, Alexandre Locquet, and D. S. Citrin. Depth resolution enhancement of terahertz deconvolution by autoregressive spectral extrapolation. *Optics Letters*, 42(9):1828–1831, May 2017.

[94] Fangfang Qu, Yi Pan, Lei Lin, Chengyong Cai, Tao Dong, Yong He, and Pengcheng Nie. Experimental and theoretical study on terahertz absorption characteristics and spectral de-noising of three plant growth regulators. *Journal of Infrared, Millimeter, and Terahertz Waves*, 39(10):1015 – 1027, 2018. Cited by: 14.

[95] Walter Nsengiyumva, Shuncong Zhong, Manting Luo, and Bing Wang. Terahertz spectroscopic characterization and thickness evaluation of internal delamination defects in gfrp composites. *Chinese Journal of Mechanical Engineering (English Edition)*, 36(1), 2023.

[96] C. Miliani, D. Domenici, C. Clementi, F. Presciutti, F. Rosi, D. Buti, A. Romani, L. Laurencich Minelli, and A. Sgamellotti. Colouring materials of pre-Columbian codices: non-invasive in situ spectroscopic analysis of the Codex Cospi. *Journal of Archaeological Science*, 39(3):672 – 679, 2012.

[97] Lindsay H. Oakley, Stephen A. Dinehart, Shelley A. Svoboda, and Kristin L. Wustholz. Identification of organic materials in his-

toric oil paintings using correlated extractionless surface-enhanced raman scattering and fluorescence microscopy. *Analytical Chemistry*, 83(11):3986 – 3989, 2011.

[98] Daniela Comelli, Austin Nevin, Gianluca Valentini, Iacopo Osticioli, Emilio Mario Castellucci, Lucia Toniolo, Davide Gulotta, and Rinaldo Cubeddu. Insights into Masolino's wall paintings in Castiglione Olona: Advanced reflectance and fluorescence imaging analysis. *Journal of Cultural Heritage*, 12(1):11 – 18, 2011.

[99] C. Miliani, F. Rosi, A. Burnstock, B.G. Brunetti, and A. Sgamellotti. Non-invasive in-situ investigations versus micro-sampling: A comparative study on a renoirs painting. *Applied Physics A: Materials Science and Processing*, 89(4):849 – 856, 2007.

[100] Winfried Denk, James H. Strickxer, and Watt W. Webb. Two-photon laser scanning fluorescence microscopy. *Science*, 248(4951):73 – 76, 1990.

[101] A.L. Gaeta and R.W. Boyd. Nonlinear optics, basics — ultrafast and intense-field nonlinear optics. In Robert D. Guenther, editor, *Encyclopedia of Modern Optics*, pages 258–262. Elsevier, Oxford, 2005.

[102] Alice Dal Fovo, Mikel Sanz, Mohamed Oujja, Raffaella Fontana, Sara Mattana, Riccardo Cicchi, Piotr Targowski, Marcin Sylwestrzak, Aldo Romani, Chiara Grazia, George Filippidis, Sotiris Psilodimitrakopoulos, Andreas Lemonis, and Marta Castillejo. In-depth analysis of egg-tempera paint layers by multiphoton excitation fluorescence microscopy. *Sustainability (Switzerland)*, 12(9), 2020.

[103] Diego Quintero Balbas, Laura Maestro-Guijarro, Paula María Carmona-Quiroga, Mohamed Oujja, Marta Castillejo, Francesca Bettini, Simone Porcinai, and Jana Striova. Non-invasive stratigraphic

analyzes of gelatine-based modern painting materials with linear and nonlinear optical methods. *JPhys Photonics*, 6(3), 2024.

[104] Gaël Latour, Jean-Philippe Echard, Marie Didier, and Marie-Claire Schanne-Klein. In situ 3D characterization of historical coatings and wood using multimodal nonlinear optical microscopy. *Optics Express*, 20(22):24623 – 24635, 2012.

[105] Emilio J. Gualda, George Filippidis, Kristalia Melessanaki, and Costas Fotakis. Third-harmonic generation and multi-photon excitation fluorescence imaging microscopy techniques for online art conservation diagnosis. *Applied Spectroscopy*, 63(3):280 – 285, 2009.

[106] D. Artigas, L. Serrado, I.G. Cormack, S. Psilodimitrakopoulos, and P. Loza-Alvarez. Prospective and applications of Two-Photon Fluorescence in archaeology and art conservation. In *Lasers in the Conservation of Artworks - Proceedings of the International Conference LACONA 7*, page 15 – 22, 2008.

[107] A. Dal Fovo, M. Sanz, S. Mattana, M. Oujja, M. Marchetti, F.S. Pavone, R. Cicchi, R. Fontana, and M. Castillejo. Safe limits for the application of nonlinear optical microscopies to cultural heritage: A new method for in-situ assessment. *Microchemical Journal*, 154, 2020.

[108] Baoju Wang, Qiuqiang Zhan, Yuxiang Zhao, Ruitao Wu, Jing Liu, and Sailing He. Visible-to-visible four-photon ultrahigh resolution microscopic imaging with 730-nm diode laser excited nanocrystals. *Opt. Express*, 24(2):A302–A311, Jan 2016.

[109] James W. M. Chon, Min Gu, Craig Bullen, and Paul Mulvaney. Three-photon excited band edge and trap emission of CdS semicon-

ductor nanocrystals. *Applied Physics Letters*, 84(22):4472–4474, 05 2004.

[110] M. Gal, L.V. Dao, E. Kraft, M.B. Johnston, C. Carmody, H.H. Tan, and C. Jagadish. Thermally stimulated luminescence in ion-implanted GaAs. *Journal of Luminescence*, 96(2):287–293, 2002.

[111] Nadia Mohammed Jassim and Nada Hadi. Nonlinear Optical Properties of CdS Semiconductor nanowires. In *IOP Conference Series: Materials Science and Engineering*, volume 454, 2018.

[112] Yoshitsugu Yamamoto, Hiroyuki Nasu, Tadanori Hashimoto, and Kanichi Kamiya. Second harmonic generation from thermally poled CdS microcrystal-containing glasses. *Journal of Non-Crystalline Solids*, 281(1-3):198 – 204, 2001.

[113] Fan Zhang, Haoran Wang, Xiongfeng Zhou, Yuqian Zhao, and Ji'an Duan. Second harmonic generation in zinc sulfide by femtosecond laser irradiation. *Optics & Laser Technology*, 127:106145, 2020.

[114] S. Enoch and H. Akhouayri. Second-harmonic specular and scattered generated light: application to the experimental study of zinc-sulfide thin films. *Appl. Opt.*, 36(25):6319–6324, Sep 1997.

[115] Hongbo Hu, Kai Wang, Hua Long, Weiwei Liu, Bing Wang, and Peixiang Lu. Precise Determination of the Crystallographic Orientations in Single ZnS Nanowires by Second-Harmonic Generation Microscopy. *Nano Letters*, 15(5):3351–3357, 2015.

[116] Daniela Comelli, Douglas MacLennan, Marta Ghirardello, Alan Phenix, Catherine Schmidt Patterson, Herant Khanjian, Markus Gross, Gianluca Valentini, Karen Trentelman, and Austin Nevin. Degradation of Cadmium Yellow Paint: New Evidence from Photoluminescence Studies of Trap States in Picasso's Femme (Époque des

"Demoiselles d'Avignon"). *Analytical Chemistry*, 91(5):3421–3428, 2019.

[117] Geert Van der Snickt, Joris Dik, Marine Cotte, Koen Janssens, Jakub Jaroszewicz, Wout De Nolf, Jasper Groenewegen, and Luuk Van der Loeff. Characterization of a Degraded Cadmium Yellow (CdS) Pigment in an Oil Painting by Means of Synchrotron Radiation Based X-ray Techniques. *Analytical Chemistry*, 81(7):2600–2610, 2009.

[118] Martin Koch, Stefan Hunsche, P. Schuacher, Martin C. Nuss, Jochen Feldmann, and J. Fromm. THz-imaging: a new method for density mapping of wood. *Wood Science and Technology*, 32:421–427, 1998.

[119] Hans W. Mocker and R. J. Collins. Mode Competition and Self-Locking Effects in a Q-Switched Ruby Laser. *Applied Physics Letters*, 7(10):270–273, 11 1965.

[120] G. P. Kniffin, Schecklman S, J. Chen, S. C. Henry, L. M. Zurk, B. Pejcinovic, and A. I. Timchenko. Measurement and modeling of terahertz spectral signatures from layered material. In G. Charmaine Gilbreath and Chadwick T. Hawley, editors, *Active and Passive Signatures*, volume 7687, page 768708. International Society for Optics and Photonics, SPIE, 2010.

[121] Corinna Ludovica Koch Dandolo and Peter Uhd Jepsen. Wall Painting Investigation by Means of Non-invasive Terahertz Time-Domain Imaging (THz-TDI): Inspection of Subsurface Structures Buried in Historical Plasters. *Journal of Infrared, Millimeter, and Terahertz Waves*, 37(2):198–208, 2015.

[122] E.S. Reyes-Reyes, R. Carriles-Jaimes, and E. Castro-Camus. Algorithm for Determination of Cutoff Frequency of Noise Floor Level

for Terahertz Time-Domain Signals. *Journal of Infrared, Millimeter, and Terahertz Waves*, 43(11-12):847 – 856, 2022.

[123] M. Oujja, F. Agua, M. Sanz, D. Morales-Martin, M. García-Heras, M.A. Villegas, and M. Castillejo. Multiphoton Excitation Fluorescence Microscopy and Spectroscopic Multianalytical Approach for Characterization of Historical Glass Grisailles. *Talanta*, 230, 2021.